Aalto University
School of Science

Hannu Laine

Modeling the Size Distribution of Iron Precipitates in Phosphorus-Implanted Silicon Solar Cells

Master's thesis submitted in partial fulfillment of the requirements for the degree of Master of Science in Technology in the Degree Program of Engineering Physics and Mathematics

Espoo 15.9.2014

Thesis supervisor:

Professor Hele Savin

Thesis instructor:

D.Sc. (Tech.) Antti Haarahiltunen

Tekijä: Hannu Laine

Työn nimi: Rautaerkaumien kokojakauman mallintaminen fosfori-istutetuissa piiaurinkokennoissa

Päivämäärä: 15.9.2014 Kieli: Englanti Sivumäärä:9+55

Mikro- ja nanotekniikan laitos

Professuuri: Micro- and Nanotechnology Koodi: S-69

Valvoja: Professor Hele Savin

Ohjaaja: TkT Antti Haarahiltunen

Keskeinen vaihe piiaurinkokennojen valmistuksessa on varauksen keräävän liitoksen valmistus. Perinteisesti liitos valmistetaan diffusoimalla seosatomeita piikiekkoon, mutta viime aikoina liitoksen luominen istuttamalla on myös herättänyt mielenkiintoa. Verrattuna perinteiseen diffuusioon, istutus on paremmin hallittavissa ja sen avulla voidaan vähentää prosessivaiheiden määrää. Vahingollisten metalliepäpuhtauksien getterointi, eli niiden haittavaikutuksen minimointi kennoprosessin aikana ei ole kuitenkaan niin laajasti ymmärrty istutetuissa kuin diffusoiduissa kennoissa. Tämä työ tutkii rautaepäpuhtauksien erkautumista ja diffuusioita tarkoituksella kontaminoiduissa piiaurinkokennoissa erilaisten lämpökäsittelyiden aikana.

Työn tulokset osoittavat, että toisin kuin diffusoiduissa kennoissa, istutetuissa kennoissa erkautuneen raudan kokonaismäärän lisäksi myös erkaumien kokojakaumalla on merkitystä, mikäli raudan negatiiviset vaikutukset halutaan minimoida. Hidas jäähdytys istutuksen aktivointilämpötilasta getterointilämpötilaan voi johtaa harvoihin, mutta isoihin rautaerkaumiin istutetulla pinnalla, mikä lisää vähemmistövarauksenkuljettajan diffuusiopituutta bulkissa, mutta saattaa vähentää kennon avoimen piirin jännitettä. Toisaalta mikäli kennot jäähdytetään nopeasti aktivaatiolämpötilasta huoneen lämpötilaan, syntyy useita, pieniä erkaumia, jotka eivät vahingoita avoimen piirin jännitettä, mutta saattavat rajoittaa diffuusiopituutta bulkissa.

Rautaerkaumien kokojakaumia tutkitaan heterogeenisellä erkaumamallilla ja simuloidut kokojakaumat vahvistetaan vertaamalla niitä synkrotroniavusteisella mikro-röntgenfluoresenssi mittauksilla. Työssä näytetään, että kokojakauma getterointiprosessin jälkeen pystytään ennustamaan, mikäli getterointiprosessin aikana bulkista vähentynyt rautakonsentraatio tiedetään etukäteen. Seuraava tutkimusaskel on ennustavan mallin kehittäminen, joka pystyisi ennustamaan rautakonsentraation vähentymisen pelkkien istutusparametrien avulla.

Avainsanat: Pii, aurinkokenno, getterointi, rauta, erkautuminen, mallinnus, istutus

Author: Hannu Laine

Title: Modeling the Size Distribution of Iron Precipitates in Phosphorus-Implanted Silicon Solar Cells

Date: 15.9.2014 Language: English Number of pages:9+55

Department of Micro- and Nanotechnology

Professorship: Mikro- ja nanotekniikka Code: S-69

Supervisor: Professor Hele Savin

Instructor: D.Sc. (Tech.) Antti Haarahiltunen

A pivotal phase in the manufacturing of crystalline silicon solar cells is the formation of the charge collecting pn-junction. Typically, the junction is created via dopant in-diffusion, but lately creating it through implantation has also raised interest. Implantation offers several potential benefits compared to diffusion, such as fewer processing steps and better process control. However, the differences between diffused and implanted junctions with respect to gettering, that is, the control of harmful metal impurities are not yet fully understood. This work studies the precipitation and diffusion of iron in intentionally iron-contaminated phosphorus-implanted silicon solar cells under varying time-temperature profiles.

In this study, it is shown that unlike in the case of diffused cells, not only the total amount of precipitated iron, but also the precipitate size distribution of iron can be important when minimizing the harmful effects of iron on the performance of implanted solar cells. A slow cooling from the implant activation temperature to a moderate gettering anneal temperature can result in few, but large iron precipitates at the implanted surface, which improves the bulk minority carrier diffusion length but reduces the open circuit voltage of the solar cell. However, by first forcing bulk precipitation by quenching the wafers to room temperature before the gettering anneal, a large number of small precipitates is formed, resulting in a high open circuit voltage.

The iron precipitate size distributions are analyzed in detail via a heterogeneous iron precipitation model and the simulation results are validated with synchrotron-based micro-X-ray fluorescence measurements. It is shown that the precipitate size distribution after the gettering anneal can be predicted, if the gettering efficiency of the gettering anneal in question is known. Thus, the next step towards predictive impurity-to-efficiency modeling of implanted cells is predicting the gettering efficiency based solely on the implantation parameters.

Keywords: Silicon, solar cell, gettering, iron, precipitation, modeling, implantation

Preface

This Master's Thesis was carried out in the Electron Physics Group at the Department of Micro and Nanosciences of Aalto University. This Thesis was a part of the project, PASSI, which received support from the Finnish Technological Agency and the following companies: Beneq Oy, Epicrystals Oy, Fortum Oyj, Luvata Pori Oy, Semilab Inc. and SolarWorld Innovations GmbH.

Firstly, I would like to express my gratitude to Professor Hele Savin for allowing me to be a part of Electron Physics Group. I am also grateful for her tireless support and the insightful advice she has given me as the supervisor of this Thesis. The instructor of this this Thesis, Antti Haarahiltunen, also played a crucial role in guiding my research into the right direction and ensuring that every minute detail of this work is scientifically sound — for that, I am much obliged.

In addition to my official supervisors, I have had the pleasure to learn from many brilliant minds during my stay at the Electron Physics Group. I am especially grateful to Ville Vähänissi, Marko Yli-Koski, Päivikki Repo, Jeanette Lindroos, Zhengjun Liu and Yameng Bao. Ville and Päivikki have also cherished me with their radiant presence in the office we have shared together.

Academic achievements are rarely solitary pursuits and this work is no exception. I am indebted to the aforementioned Ville Vähänissi for processing the samples analyzed in this work. The newly reported open circuit voltage values were also measured by him. Furthermore, the X-ray fluorescence measurements were performed by David P. Fenning, Ashley E. Morishige, Jasmin Hofstetter, Mallory A. Jensen and Sergio Casellanos from the Photovoltaic Laboratory of Massachusetts Institute of Technology. David and Ashley also participated in the data analysis — it has been a pleasure collaborating with you!

This Thesis and the arduous studies preceding it would not have been possible without the unconditional support from my parents that I have been blessed with throughout my life. I am also thankful for the many friends I have had the luck to be surrounded by. Especially Milka, Paula and my sister Siiri have provided me an abundance of laughter and joy to balance my studies and work. Lastly, I want to express my gratitude to my wife, Aino, for being the best imaginable companion in this wonderful adventure that is life.

Espoo, September 15th, 2014

Hannu Laine

Contents

Abstract (in Finnish) ii

Abstract iii

Preface iv

Contents v

Symbols and abbreviations vii

1 Introduction 1

2 Gettering simulator for iron in crystalline silicon 2
- 2.1 Silicon bandgap and Fermi level 2
  - 2.1.1 Intrinsic silicon 2
  - 2.1.2 Doped silicon 4
- 2.2 Behavior of iron in intrinsic silicon 5
- 2.3 Effect of boron doping on diffusivity and solubility of iron 6
- 2.4 Effect of phosphorus doping on diffusivity and solubility of iron 9
- 2.5 Precipitation of iron 10
- 2.6 Structure and computational aspects of the simulator 13
- 2.7 Nucleation and precipitation parameters 16

3 Experimental methods used to study iron in silicon wafers 19
- 3.1 Quantifying the interstitial iron concentration by the surface photovoltage method 19
  - 3.1.1 Measurement setup in the SPV method 19
  - 3.1.2 Gauging the minority carrier diffusion length 20
  - 3.1.3 Determining the interstitial iron concentration 22
- 3.2 Quantifying the distribution of iron precipitates by synchrotron-based micro-X-ray fluorescence 23
  - 3.2.1 X-ray fluorescence as an electronic process 23
  - 3.2.2 Measurement setup and information depth of the µ-XRF technique 25
  - 3.2.3 Discerning iron precipitates from µ-XRF data maps 26

4 Wafer treatments studied in this work 27
- 4.1 Sample preparation and gettering anneals 27
- 4.2 Preliminary experimental findings: importance of precipitation 29

5 Simulation results 31
- 5.1 Hypothesis: Macroscopic effect caused by precipitate size distribution . . 31
- 5.2 Density of precipitation sites in non-implanted silicon 31
- 5.3 Gettering properties of the implanted emitter 33
  - 5.3.1 Assessment of assumptions for SPV measurements 36

5.4 Simulated precipitate size distributions after processing 38
5.4.1 Precipitates at the emitter 38
5.4.2 Precipitates in the bulk 40

6 Verification of simulation results by the μ-XRF method **42**
6.1 Distinguishing precipitates from noise 42
6.2 Comparing simulated and measured precipitate size distributions at the emitter 46

7 Conclusions **48**

References **49**

Appendix A **54**

Symbols and abbreviations

Symbols

$\alpha(\lambda)$	Wavelength dependent absorption coefficient of photons
$[B^-]$	Concentration of ionized boron
$C_n(Fe_i)$	Electron capture coefficient of interstitial iron
$C_n(FeB)$	Electron capture coefficient of iron boron pairs
C_{SPV}	Calibration constant of the surface photovoltage method
D	Full-width half maximum diameter of the primary X-ray beam in μ-XRF
D_C	Density of states in the conduction band of silicon
D_{Fe}	Diffusivity of interstitial iron
D_{Fe}^{int}	Diffusivity of interstitial iron in intrinsic silicon
D_{Fe}^{n}	Diffusivity of interstital iron in n-doped silicon
D_{Fe}^{p+}	Effective diffusivity of interstitial iron in p+ doped silicon
$D_{Fe^+}^{p+}$	Diffusivity of ionized interstitial iron in p+ doped silicon
D_L	Minority carrier diffusion length
D_n	Minority carrier diffusivity
D_V	Density of states in the valence band of silicon
d	Wafer thickness in the SPV method
d_{inf}	Effective information depth of the μ-XRF measurement setup
$d(n,t)$	Time dependent particle flux out from an iron precipitate with n atoms
d_1	1/e attenuation length of the primary XRF beam in silicon
d_2	1/e attenuation length of the secondary XRF beam in silicon
E	Energy
E_a	Iron precipitation simulation parameter
E_C	Energy at the lower edge of the conduction band of silicon
E_D	Energy at the iron donor level
E_F	Fermi level of silicon
E_F^{int}	Fermi level of intrinsic silicon
E_F^{p+}	Fermi level in p+ doped silicon
E_g	Bandgap of silicon
E_g^{int}	Bandgap of intrinsic silicon
E_V	Energy at the higher edge of the valence band of silicon
ε_{Si}	Permittivity of silicon
$[Fe_i]$	Total concentration of interstitial iron
$[Fe]_{FeSi_2}$	Total concentration of iron in $FeSi_2$ precipitates
$[Fe_i^+]$	Concentration of ionized interstitial iron
$[Fe_i^+]_{p+}$	Concentration of ionized interstitial iron in p+ doped silicon
$[Fe_i^+]_{int}$	Concentration of ionized interstitial iron in intrinsic silicon
$[Fe_i^0]$	Concentration of neutral interstitial iron
$[Fe_i^0]_{p+}$	Concentration of neutral interstitial iron in p+ doped silicon
$[Fe_i^0]_{int}$	Concentration of neutral interstitial iron in intrinsic silicon
$[Fe_i^+B^-]$	Concentration of iron boron pairs

f_{diss}	Fraction of dissociated iron boron pairs
$f(n,t)$	Time dependent size distribution of iron precipitates
f_{FD}	Fermi-Dirac distribution
f_{Fe}	Fraction of ionized interstitial iron
ΔG	Change in Gibbs free energy
G	Minority carrier generation rate
$g(n,t)$	Time dependent particle flux in to an iron precipitate with n atoms
$I(x)$	Depth dependent intensity of the X-ray beam in μ-XRF
I_0	Initial intensity of the X-ray beam in μ-XRF
J_{eff}	Effective iron flux during iron diffusion
j_{nm}	Rate of change for an iron precipitate cluster size from n atoms to m atoms
$K_n(t)$	Occuring rate for non-aggregative growth processes of iron precipitates
k_{B}	Boltzmann constant
k_{seg}	Segregation coefficient of iron
L_{Fe}	μ-XRF pixel loading in $\mu g/cm^2$
$L_n(t)$	Occuring rate for non-aggregative dissolution processes of iron precipitates
L_1	Minority carrier diffusion length measured before the dissociation of iron boron pairs
L_2	Minority carrier diffusion length measured after the dissociation of iron boron pairs
M_{Fe}	Molar mass of iron
$M(t)$	Time dependent largest cluster size of the simulated iron precipitation system
μ/ρ	Energy dependent mass absorption coefficient of X-rays
N_{A}	Avogadro's constant
N_{a}	Acceptor type dopant concentration
N_{atoms}	μ-XRF pixel loading in atoms per pixel
$N_{\text{C}}^{\text{eff}}$	Effective density of states in the conduction band of silicon
N_{ox}	Density of oxide precipitates
N_{p}	Density of iron precipitates
N_{site}	Density of iron precipitation sites
$N_{\text{V}}^{\text{eff}}$	Effective density of states in the valence band of silicon
Δn	Excess minority carrier concentration
n	Size of an iron precipitate in atoms
n_e	Electron concentration in the conduction band of silicon
n_{po}	Equlibrium electron density in p-doped silicon
Ω	Pairing constant of iron boron pairs
[P]	Phosphorus concentration
p	Hole concentration in the valence band of silicon
p_0	Equilibrium hole concentration in the valence band of silicon
p_1	Iron nucleation simulation parameter
Φ	Photon flux density
q	Electron charge
R	Reflectivity of the SPV sample surface
R_{C}	Capture radius of mobile Fe^+ ions by B acceptors
r_{c}	Capture radius of iron precipitates
r_{ox}	Capture radius of oxide precipitates
r_0	Capture radius of iron precipitation sites

ρ	Mass density
S_{Fe}	Solid solubility of iron in silicon
$S_{\mathrm{Fe}}^{\mathrm{max}}$	Operator for determining the maximum solubility of iron in neighbouring nodes
$S_{\mathrm{Fe}}^{\mathrm{int}}$	Solid solubility of iron in intrinsic silicon
$S_{\mathrm{Fe}}^{\mathrm{n+}}$	Solid solubility of iron in n+ doped silicon
$S_{\mathrm{Fe}}^{n}(n)$	Size dependent equilibrium concentration for the dissolution of iron precipitates
$S_{\mathrm{Fe}}^{\mathrm{p+}}$	Solid solubility of iron in p+ doped silicon
S_{Fe}^{0}	Solid solubility of neutral iron in silicon
s_r	Surface recombination velocity at the front surface of the SPV sample
s_1	Surface recombination velocity at the edge of space-charge region in SPV
T	Temperature
V_{OC}	Open circuit voltage
V_{SPV}	Surface photovoltage voltage
τ_{C}	Time constant of the association of iron boron pairs
τ_{diss}	Time constant of the dissociation of iron boron pairs
τ_n	Minority carrier lifetime
W	Width of the space-charge region in SPV

Abbreviations

EBIC	Electron beam induced current
eV	Electron volt
FPE	Fokker-Planck equation
FWHM	Full-width half maximum
μ-XRF	micro-X-ray fluorescence
scr	Space-charge region
SIMS	Secondary ion mass spectrometry
SPV	Surface photovoltage
TEM	Transmission electron microscopy

1 Introduction

Implantation has recently raised interest in the silicon solar cell industry as a method to create the emitter in p-type solar cells. Compared to the traditional phosphorus in-diffusion, it offers the potential for fewer processing steps and better process control [1]. Better control of the emitter doping profile can be utilized in achieving higher blue response, lower front surface recombination velocity and a selective emitter [2]. Ultimately, implantation could provide a pathway to low-cost high-efficiency solar cells.

However, one of the important benefits of phosphorus in-diffusion is the segregation of iron impurities to the phosphorus-doped layer [3]. Gettering of iron, i.e. the reduction of iron impurities from the bulk of the wafer is important because iron can act as a recombination center for charge carriers and limit the bulk minority charge carrier diffusion length and, ultimately, the cell efficiency [4]. Thus, the gettering of iron in the presence of an implanted emitter is currently under investigation [5].

Recent gettering tests with intentionally iron contaminated samples have revelaed that when gettering iron in p-type silicon with a phosphorus implanted emitter, a higher initial iron concentration can lead to lower interstitial iron concentration after processing [5]. This suggests that precipitation plays a role in the gettering process. In addition, the interstitial iron concentration level remained higher than the solid solubility of iron in all studied gettering anneal temperatures [6, 7] suggesting that if also segregation has a role, its effect is smaller than when gettering with a diffused emitter [8].

The purpose of this study is to further elucidate the gettering mechanisms when gettering iron with an implanted emitter. The previously studied gettering anneals and their gettering efficiencies [5] are scrutinized and the roles of both segregation and precipitation in the gettering process are assessed with the help of a heterogeneous iron precipitation model [9]. Newly measured open circuit voltage values in fully processed ion-implanted cells are reported which further indicate that not only the total amount of iron precipitated, but also the size distribution of iron precipitates may have an effect on macroscopic cell parameters. The iron precipitate size distributions are simulated after various gettering anneals and the size distributions are correlated with the measured open circuit voltages and the previously reported bulk minority charge carrier diffusion lengths [5].

By experimentally verifying the size distributions by synchrotron-based micro-X-ray fluorescence (μ-XRF), it is shown that the precipitate size distributions can be predicted to a certain extent. Necessary future steps are highlighted to reach a truly predictive impurity-to-efficiency model [10] capable of modeling quantified cell parameters based solely upon the contamination level of the starting material and the process parameters for the implanted solar cells. This predictive model could facilitate quick and cost-efficient process optimization by eliminating the need for expensive experimental tests.

2 Gettering simulator for iron in crystalline silicon

The behavior of iron in silicon has been studied extensively [11, 12] due to its harmful effect on solar cell performance [13] and prevalence in silicon feedstocks [14] and throughout the industrial processing environment [15, 16]. Iron gettering is the art of reducing the negative impact of iron on the performance of solar cells.

Gettering of iron can be divided into two main mechanisms: internal and external gettering. Internal gettering of iron refers to precipitation of iron, that is, the reduction of interstitial iron through the formation of iron-silicide precipitates. Because iron-silicide precipitates typically contain many iron atoms, they can be scattered sparsely, such that their net effect on the performance of solar cells is smaller than if the same amount of iron would be scattered as individual iron atoms in interstitial form. External gettering, on the other hand, refers to the increase of iron solubility in specifid portions of the silicon wafer, for example near the surface, which results in segregation of interstitial iron away from the wafer bulk towards the wafer surface, where iron is less detrimental to cell performance. External gettering often occurs naturally during the emitter formation, at least for emitters created with phosphorus in-diffusion [17].

When optimizing the gettering properties of the cell manufacturing process to match the desired efficiency and cost requirements based on the contamination level of the starting material, simulations can be used to guide the pilot experiments [18]. This can lead to streamlined experimental tests saving both time and money.

This section presents the structure and the physical basis of the gettering simulator used in this work.

2.1 Silicon bandgap and Fermi level

To be able to model the behavior of iron in silicon, the material properties of silicon need to be understood. This section introduces those properties of both intrinsic and doped silicon, which are relevant to the simulator used in this work.

2.1.1 Intrinsic silicon

The temperature dependence of the bandgap of intrinsic silicon E_g^{int} is given by the semi-empirical formula [19]:

$$E_g^{int} = E_C - E_V = 1.17 - \frac{4.9 \cdot 10^{-4} \cdot T^2}{T + 655} \text{ [eV]}, \tag{1}$$

where E_C and E_V are the energies at the lower edge of the conduction band and the higher edge of the valence band respectively, T is temperature and eV electron volt. It should be

noted that Eq. (1) was only verified for temperatures below 750 K. The charge carrier densities in the conduction and valence bands are determined by Fermi-Dirac statistics:

$$n_e = \int_{E_\mathrm{C}}^{\infty} D_\mathrm{C}(E) f_{FD}(E,T)\mathrm{d}E, \tag{2}$$

$$p = \int_{\infty}^{E_\mathrm{V}} D_\mathrm{V}(E)\left[1 - f_{FD}(E,T)\right]\mathrm{d}E, \tag{3}$$

where n_e is the electron concentration in the conduction band and p is the hole concentration in the valence band, D_C and D_V are the densities of states in the conduction and valence bands, respectively, and f_FD is the Fermi-Dirac distribution determining the occupation probability of an electron state at energy E:

$$f_\mathrm{FD}(E,T) = \frac{1}{\exp\left[\left(E - E_\mathrm{F}\right)/k_\mathrm{B}T\right] + 1}, \tag{4}$$

where E_F is the Fermi level and k_B the Boltzmann constant. Typically for silicon, the parabolic approximation is made, that is, it is assumed that the effective masses of the charge carriers remain constant. Furthermore, for intrinsic and moderately doped silicon, the Fermi-Dirac distribution can be approximated with Boltzmann statistic and Eqs. (2) and (3) can be expressed as [20]:

$$n_e = N_\mathrm{C}^\mathrm{eff}(T)\exp\left(-\frac{E_\mathrm{C} - E_\mathrm{F}}{k_\mathrm{B}T}\right), \tag{5}$$

$$p = N_\mathrm{V}^\mathrm{eff}(T)\exp\left(\frac{E_\mathrm{V} - E_\mathrm{F}}{k_\mathrm{B}T}\right), \tag{6}$$

where $N_\mathrm{C}^\mathrm{eff}$ and $N_\mathrm{V}^\mathrm{eff}$ are the effective densities of states in the conduction and valence band, respectively. In this work, values for the densities of states are taken from [21]. The intrinsic Fermi level $E_\mathrm{F}^\mathrm{int}$ adopts a position such that charge neutrality $n_e = p$ is satisfied:

$$E_\mathrm{F}^\mathrm{int} = \frac{E_\mathrm{g}^\mathrm{int}}{2} - \frac{1}{2}k_\mathrm{B}T\ln\frac{N_\mathrm{V}}{N_\mathrm{C}}. \tag{7}$$

From Eqs. (5)-(7), the intrinsic charge carrier concentration $n_\mathrm{i} = n_e = p$ is readily solved:

$$n_\mathrm{i} = \sqrt{N_\mathrm{C}N_\mathrm{V}}\exp\left(\frac{-E_\mathrm{g}}{2k_\mathrm{B}T}\right). \tag{8}$$

2.1.2 Doped silicon

Under doping both E_g and E_F understandably change and are no longer given by Eqs. (1) and (7). For E_g, doping induced bandgap narrowing [22] is added to yield a final expression for non-degenerate p-type silicon:

$$E_g = E_C - E_V = 1.17 \text{ eV} - \frac{4.9 \cdot 10^{-4} \cdot (T^2/\text{K}^2) \text{ eV}}{T/\text{K} + 655} - \frac{3q^2}{16\pi\varepsilon_{\text{Si}}} \left(\frac{q^2 p}{\varepsilon_{\text{Si}} k_B T} \right)^{1/2}, \tag{9}$$

where q is the electron charge and ε_{Si} the permittivity of silicon. For non-degenerate, p-type silicon under the Boltzmann approximation, the hole concentration can be expressed with the help of the charge neutrality condition and mass action law [20]:

$$p = N_a + n_e, p = \frac{n_i^2}{n} \tag{10}$$

$$\Rightarrow p = \frac{N_a}{2} + \left[\left(\frac{N_a}{2} \right)^2 + n_i^2 \right]^{1/2}, \tag{11}$$

where N_a is the acceptor type dopant concentration and it is assumed that all dopants are ionized. Under high doping, the relation between Fermi-energy and the hole concentration cannot be described by the Boltzmann approximation (Eq. (6)), but instead Fermi-Dirac statistics (Eq. (3)) has to be used. To facilitate this, Eq. (3) can be expressed with the help of a power series as [23]:

$$E_F - E_V = -k_B T \left[\ln \frac{p}{N_V^{\text{eff}}} + \sum_{i=1}^{\infty} A_i \left(\frac{p}{N_V^{\text{eff}}} \right)^i \right], \tag{12}$$

where the coefficients A_i are constants. In this work, the summation in Eq. (12) is truncated after the fourth term to reach acceptable accuracy without unnecessary computational load. Under the parabolic approximation, the values of the first four coefficients A_i are [23]:

$$A_1 = \frac{1}{4} 2^{1/2} \tag{13}$$

$$A_2 = \frac{3}{16} - \frac{1}{9} 3^{1/2} \tag{14}$$

$$A_3 = \frac{1}{8} + \frac{5}{48} 2^{1/2} - \frac{1}{9} 6^{1/2} \tag{15}$$

$$A_4 = \frac{1585}{6912} + \frac{5}{32} 2^{1/2} - \frac{5}{24} 3^{1/2} - \frac{1}{25} 5^{1/2}. \tag{16}$$

A self-consistent solution for Eq. (12) is acquired with the following iterative algorithm:

0. As a starting value, solve p^0 from Eq. (11) and then based on p^0, solve E_F^0 with the help of Eq. (12).
1. Solve n^n based on E_F^{n-1} with the help of Eq. (2).
2. Assume all acceptors to be ionized and solve p^n by $p^n = n_e^n + N_a$.
3. Solve E_F^{n+1} based on p^n with the help of Eq. (12).
4. Set $E_F^{n+1} = \left(E_F^{n+1} + E_F^n\right)/2$.
5. Go back to step 1.

In this work, this algorithm is typically repeated over 3 cycles.

2.2 Behavior of iron in intrinsic silicon

Typical solar cells are doped throughout the wafer, but the theory of iron behavior under doping is largely based on the behavior of iron in intrinsic silicon. This section discusses the properties of iron in intrinsic silicon relevant to modeling iron gettering: the charge state of interstitial iron, the position of the donor level of interstitial iron in the silicon bandgap, the diffusivity of interstitial iron and the solid solubility of iron.

Interstitial iron can be present in neutral or ionized form depending whether the donor level formed by the interstitial atom is occupied by a hole or an electron. The ratio of the concentration of these two species can be derived with the help of statistical physics [24] or alternatively using Fermi-Dirac statistics and probability theory as shown in Appendix A:

$$\frac{[\mathrm{Fe}_i^+]}{[\mathrm{Fe}_i^0]} = \frac{1}{2}\exp\left[\left(E_D - E_F\right)/k_B T\right], \tag{17}$$

where $[\mathrm{Fe}_i^+]$ is the concentration of ionized interstitial iron and $[\mathrm{Fe}_i^0]$ is the concentration of neutral interstitial iron. In this work, the iron donor level E_D is calculated using a piecewise defined function based on experimental data [21]:

$$E_D - E_V = \begin{cases} 2.956 \cdot 10^{-5} \cdot (T/\mathrm{K}) + 0.38\ [\mathrm{eV}],\ T \leq 1015\ \mathrm{K} \\ 1.6522 - 1.224 \cdot 10^{-3} \cdot (T/\mathrm{K})\ [\mathrm{eV}],\ 1015\ \mathrm{K} < T \leq 1350\ \mathrm{K} \\ 0,\ T > 1350\ \mathrm{K}. \end{cases} \tag{18}$$

As to the diffusivity of interstitial iron, Istratov *et al.* [11] gathered iron diffusivity data from various experiments performed in temperatures ranging from 250 °C to 1200 °C. Regardless of the charge state of iron in the measurement temperatures, a single Arrhenius

plot could be fitted through all the data points yielding for the diffusivity of iron in intrinsic silicon $D_{\mathrm{Fe}}^{\mathrm{int}}$:

$$D_{\mathrm{Fe}}^{\mathrm{int}} = 1 \cdot 10^{-3} \exp\left(\frac{-0.67\ \mathrm{eV}}{k_{\mathrm{B}}T}\right) [\mathrm{cm}^2/\mathrm{s}]. \tag{19}$$

For the solid solubility of iron in intrinsic silicon, this work combines the results of Aoki *et al.* [6] and Muprhy *et al.* [7] resulting in a piecewise defined solubility:

$$S_{\mathrm{Fe}}^{\mathrm{int}} = \begin{cases} 4.3 \cdot 10^{22} \exp\left(\frac{-2.1\ \mathrm{eV}}{k_{\mathrm{B}}T}\right) [\mathrm{cm}^{-3}], T > 700°\mathrm{C} \\ 1.2 \cdot 10^{21} \exp\left(\frac{-1.8\ \mathrm{eV}}{k_{\mathrm{B}}T}\right) [\mathrm{cm}^{-3}], T \leq 700°\mathrm{C}. \end{cases} \tag{20}$$

2.3 Effect of boron doping on diffusivity and solubility of iron

In boron doped regions of silicon where iron is present, $\mathrm{Fe_iB}$ pairs are formed. Thus, iron can be present in four forms: paired with boron, charged interstitial form, neutral interstitial form and in iron-silicide precipitates. The amount of each iron species present depends on the equilibrium reactions:

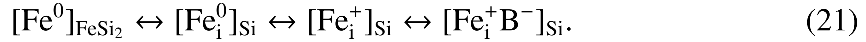

$$[\mathrm{Fe}^0]_{\mathrm{FeSi_2}} \leftrightarrow [\mathrm{Fe_i^0}]_{\mathrm{Si}} \leftrightarrow [\mathrm{Fe_i^+}]_{\mathrm{Si}} \leftrightarrow [\mathrm{Fe_i^+B^-}]_{\mathrm{Si}}. \tag{21}$$

In Eq. (21) the equilibrium ratio of the first reaction is determined by the solid solubility of iron given by Eq. (20). The ratio of the concentrations of neutral and positively charged iron is determined by the Fermi-level as stated in Eq. (17) and the concentration of iron-boron pairs $[\mathrm{Fe_i^+B^-}]$ is determined by the mass action relationship [25, 26]:

$$\frac{[\mathrm{Fe_i^+B^-}]}{[\mathrm{Fe_i^+}][\mathrm{B^-}]} = \frac{4}{5 \cdot 10^{22}} \exp\left(\frac{0.65\ \mathrm{eV}}{k_{\mathrm{B}}T}\right), \tag{22}$$

where $[\mathrm{B^-}]$ is the concentration of ionized boron, which is assumed to equal the total boron density throughout this work. Furthermore, the solubility of neutral iron S_{Fe}^{0} is assumed to remain constant, which can be calculated with the help of Eqs. (17) and (20) through the expression:

$$S_{\mathrm{Fe}}^{0} = S_{\mathrm{Fe}}^{\mathrm{int}} \frac{[\mathrm{Fe_i^+}]}{[\mathrm{Fe_i^0}]}. \tag{23}$$

When iron is doped by boron, the solubility of iron is increased by two mechanisms: the solubility of charged iron is enhanced by the lowered Fermi-level as predicted by Eq. (17) and the solubility of iron is enhanced by the formation of $\mathrm{Fe_iB}$ pairs as stated by Eq. (22). With the help of Eqs. (17) and (22), the expression for the total iron solubility in p+ silicon $S_{\mathrm{Fe}}^{\mathrm{p+}}$ becomes:

$$S_{\text{Fe}}^{\text{p+}} = [\text{Fe}_\text{i}^0] + [\text{Fe}_\text{i}^+] + [\text{Fe}_\text{i}^+\text{B}^-] \tag{24}$$

$$= [\text{Fe}_\text{i}^0] + [\text{Fe}_\text{i}^0]\frac{1}{2}\exp\left(\frac{E_\text{D} - E_\text{F}}{k_\text{B}T}\right) + [\text{Fe}_\text{i}^+][\text{B}^-]\frac{4}{5\cdot 10^{22}\ \text{cm}^{-3}}\exp\left(\frac{0.65\ \text{eV}}{k_\text{B}T}\right) \tag{25}$$

$$= [\text{Fe}_\text{i}^0]\left\{1 + \frac{1}{2}\exp\left(\frac{E_\text{D} - E_\text{F}}{k_\text{B}T}\right)\left[1 + \frac{4[\text{B}^-]}{5\cdot 10^{22}\ \text{cm}^{-3}}\exp\left(\frac{0.65\ \text{eV}}{k_\text{B}T}\right)\right]\right\}. \tag{26}$$

Now, if it is asumed that the solubility of neutral iron remains constant regardless of boron doping, $[\text{Fe}_\text{i}^0]$ can be solved from Eq. (26) with the help of Eq. (23) to yield the following expression for $S_{\text{Fe}}^{\text{p+}}$:

$$S_{\text{Fe}}^{\text{p+}} = S_{\text{Fe}}^{\text{int}}\frac{1 + \frac{1}{2}\exp\left(\frac{E_\text{D} - E_\text{F}^{\text{p+}}}{k_\text{B}T}\right)\left[1 + \frac{4[\text{B}^-]}{5\cdot 10^{22}\ \text{cm}^{-3}}\exp\left(\frac{0.65\ \text{eV}}{k_\text{B}T}\right)\right]}{1 + \frac{1}{2}\exp\left(\frac{E_\text{D} - E_\text{F}^{\text{int}}}{k_\text{B}T}\right)}, \tag{27}$$

where $E_\text{F}^{\text{p+}}$ and E_F^{int} refer to the Fermi-level in the p+ region and the intrinsic region of the silicon wafer, respectively. The segregation coefficient k_{seg} is defined as the ratio of the iron solubilities in the highly p-doped region and the bulk of the silicon wafers:

$$k_{\text{seg}} = \frac{S_{\text{Fe}}^{\text{p+}}}{S_{\text{Fe}}^{\text{int}}} = \frac{[\text{Fe}_\text{i}^+]_{\text{p+}} + [\text{Fe}_\text{i}^0]_{\text{p+}} + [\text{Fe}_\text{i}^+\text{B}^-]}{[\text{Fe}_\text{i}^+]_{\text{int}} + [\text{Fe}_\text{i}^0]_{\text{int}}}, \tag{28}$$

where the subscripts "int" and "p+" refer to the concentrations of the different iron species in intrinsic and p+ regions of the silicon wafer, respectively. Assuming that the neutral iron concentration is the same in both species, the segregation coefficient can be expressed with the help of Eqs. (17) and (22) as:

$$k_{\text{seg}} = \frac{1 + \frac{1}{2}\exp\left(\frac{E_\text{D} - E_\text{F}^{\text{p+}}}{k_\text{B}T}\right)\left[1 + \frac{4[\text{B}^-]}{5\cdot 10^{22}\ \text{cm}^{-3}}\exp\left(\frac{0.65\ \text{eV}}{k_\text{B}T}\right)\right]}{1 + \frac{1}{2}\exp\left(\frac{E_\text{D} - E_\text{F}^{\text{int}}}{k_\text{B}T}\right)}, \tag{29}$$

where $E_\text{F}^{\text{p+}}$ and E_F^{int} refer to the Fermi-level in the p+ and intrinsic region of the silicon wafer, respectively.

In addition to the changes in iron solubility, the formation of iron-boron pairs also affects the diffusivity of iron. Because the pair formation only affects the positively charged iron, the diffusivity of the neutral iron remains the same as in intrinsic silicon and is given by Eq. (19). The effective diffusivity of iron in boron doped silicon is thus:

$$D_{\text{Fe}}^{\text{p+}} = f_{\text{Fe}}\cdot D_{\text{Fe}^+}^{\text{p+}} + (1 - f_{\text{Fe}})\cdot D_{\text{Fe}}^{\text{int}}, \tag{30}$$

where f_{Fe} is the fraction of ionized iron of all interstitial iron and $D^{\mathrm{p+}}_{\mathrm{Fe}^+}$ is the diffusivity of positively charged iron in the presence of boron. $D^{\mathrm{p+}}_{\mathrm{Fe}^+}$ can be solved by observing the pairing kinetics of iron and boron. In addition to Eq. (22), another way to express the mass action relationship of $\mathrm{Fe_iB}$ pairs is through the ratio of the concentrations of paired and unpaired ions [27]:

$$\frac{[\mathrm{Fe_i^+B^-}]}{([\mathrm{Fe_i^+B^-}]-[\mathrm{B^-}])^2} = \Omega, \tag{31}$$

where Ω is the pairing constant of $\mathrm{Fe_iB}$ pairs. Under the assumption $[\mathrm{Fe_i^+}] \ll [\mathrm{B^-}]$, it can be shown that [27, 28]:

$$\Omega = \frac{\tau_{\mathrm{C}}^{-1}}{[\mathrm{B^-}]\tau_{\mathrm{diss}}^{-1}} = \frac{4\pi D^{\mathrm{int}}_{\mathrm{Fe}} R_{\mathrm{C}}}{\tau_{\mathrm{diss}}^{-1}}, \tag{32}$$

where τ_{C} and τ_{diss} are, respectively, the temperature dependent time constants of association and dissociation of $\mathrm{Fe_iB}$ pairs, and R_{C} is the capture radius of mobile $\mathrm{Fe^+}$ ions by B acceptors. With further utilization of the assumption $[\mathrm{Fe_i^+}] \ll [\mathrm{B^-}]$, the diffusivity of posivite iron in p-doped silicon can be approximated as [27]:

$$D^{\mathrm{p+}}_{\mathrm{Fe}^+} = \frac{D^{\mathrm{int}}_{\mathrm{Fe}}}{1+\Omega[\mathrm{B^-}]}. \tag{33}$$

Combining Eqs. (32) and (33) yields:

$$D^{\mathrm{p+}}_{\mathrm{Fe}^+} = \frac{D^{\mathrm{int}}_{\mathrm{Fe}}}{1+4\pi D^{\mathrm{int}}_{\mathrm{Fe}} R_{\mathrm{C}} \tau_{\mathrm{diss}} [\mathrm{B^-}]}. \tag{34}$$

Similar approach for the calculation of the diffusivity of iron in presence of boron has been utilized before [29]. In this work, τ_{diss} is calculated as [30]:

$$\tau_{\mathrm{diss}} = 9.35 \cdot 10^{-16} \exp\left(\frac{1.40\ \mathrm{eV}}{k_{\mathrm{B}}T}\right)\ \ [\mathrm{s}]\,. \tag{35}$$

The capture radius R_{C} is solved from the condition that the average thermal energy $k_{\mathrm{B}}T$ has to equal the attractive potential energy $V(r)$ at the capture radius. As R_{C} is typically as large as several nm, the covalent component of the ion interaction can be neglected and $V(R_{\mathrm{C}})$ can be approximated by a screened Coulomb potential [28]:

$$k_{\mathrm{B}}T = \frac{q^2}{4\pi\varepsilon_{\mathrm{Si}} R_{\mathrm{C}}} \exp\left[-R_{\mathrm{C}} \middle/ \left(\frac{\varepsilon_{\mathrm{Si}} k_{\mathrm{B}} T}{q^2 p}\right)\right], \tag{36}$$

where the exponential term accounts for the screening induced by the holes and the fraction in front of the exponential term is the standard Coulomb potential. In the simulator, R_C is solved by taking a 4. order Taylor's approximation of the exponential term in Eq. (54) and solving the resulting polynomial equation in order to reduce computational load.

2.4 Effect of phosphorus doping on diffusivity and solubility of iron

Unlike for boron doping, there is not a widely accepted theory for the effect of phosphorus doping on diffusivity and solubility of iron. In phosphorus-doped silicon, interstitial iron remains neutral, which makes similar pairing reaction with phosphorus far less likely as with boron [31]. In [32], a possible model for phosphorus segregation is presented, where a doubly negative vacancy V^{--} reacts with a neutral interstitial iron atom creating a negatively charged substitional iron Fe_s^- atom and an electron e:

$$V^{--} + Fe_i^0 \leftrightarrow Fe_s^- + e. \tag{37}$$

Subsequently, the charged substitional iron atom reacts with an ionized phosphorus atom resulting in an Fe_sP -pair:

$$Fe_s^- + P^+ \leftrightarrow Fe_sP. \tag{38}$$

Using this model and the values presented in [32], for example a phosphorus doping of [P]=10^{20} cm^{-3} would result in an iron solubility of approximately $1.7 \cdot 10^{17}$ cm^{-3} at 700 °C. However in [33], the solubility of iron under a phosphorus doping of [P]=10^{20} cm^{-3} was measured to be $(6\pm2) \cdot 10^{14}$ cm^{-3} at 700 °C, almost three decades less than the presented model predicts. According to Eq. (26), solubility of iron under boron doping of [B]=10^{20} cm^{-3} is approximately $5.1 \cdot 10^{14}$ cm^{-3} at 700 °C. Thus, in this work it is assumed that the temperature and doping dependance of iron solubility under phosphorus doping behaves approximately as Eq. (26) predicts. Note that the actual physical process leading up to the increased solubility most likely differs for the case of boron and phosphorus. The boron model is merely used as a tool to roughly estimate the temperature and doping dependence of phosphorus segregation in the wafers studied in this work.

As to the effect of phosphorus doping on iron diffusivity, it is assumed that the increased solubility of iron is due to an increased concentration of immobile Fe species [33]. Thus, the effective diffusivity of iron in n-type silicon $D_{\text{eff}}^{\text{n}}$ is lowered as the solubility is increased:

$$D_{\text{Fe}}^{\text{n+}} = \frac{D_{\text{int}}}{k_{\text{seg}}} = D_{\text{int}} \frac{S_{\text{Fe}}^{\text{int}}}{S_{\text{Fe}}^{\text{n+}}}, \tag{39}$$

where S_{Fe}^{n} is iron solubility in n-type silicon.

2.5 Precipitation of iron

When the dissolved iron concentration in silicon surpasses the solid solubility of iron, iron begins to precipitate in iron-silicide clusters. The extent, to which the solid solubility is surpassed, is defined as the level of supersaturation, $\ln\left(k_B T[\mathrm{Fe_i}]/S_{\mathrm{Fe}}\right)$. The nucleation and growth of the precipitates is described by the time dependent size distribution of the precipitates $f(n,t)$, where $f(n,t)$ refers to the density of precipate of size n at time t. The size of a cluster changes from n to m with a frequency j_{nm}, which is generally time dependent. In general, there can also be non-aggregative processes occuring at certain rates which shall be denoted by $K_n(t)$ and $L_n(t)$. Accounting for all the possible growth and dissolution methods of the precipitates, the evolution of the size distribution can be investigated by the master equation of first-order phase transitions in one-component systems [34]:

$$\frac{\mathrm{d}}{\mathrm{d}t} f(n,t) = -\sum_{m=1}^{M(t)} \left[j_{mn}(t) f_m(t) - j_{nm}(t) f_n(t) \right] + K_n(t) - L_n(t), \tag{40}$$

where $M(t)$ is the (time dependent) largest cluster size of the system. In this work, the following assumptions are made:

1. Clusters can grow or dissolve only by aggregative processes, i.e. $K_n(t) = 0$ and $L_n(t) = 0$.
2. Clusters can grow or dissolve only by losing or gaining single iron atoms, i.e. $j_{nm} = 0$, for $|n - m| > 1$. In other words, it is assumed that clusters with more than one atom do not coalesce into each other.

With these assumptions, Eq. (40) can be transformed into the form of the Fokker-Planck equation (FPE) [35]:

$$\frac{\partial}{\partial t} f(n,t) = \frac{\partial}{\partial n} \left\{ -\left[g(n,t) - d(n,t) \right] f(n,t) + \frac{1}{2} \left[g(n,t) + d(n,t) \right] \frac{\partial}{\partial n} f(n,t) \right\}, \tag{41}$$

where $g(n,t)$ and $d(n,t)$ describe the particle flux in and out of the precipitates, respectively. In Eq. (41), the term $g(n,t) - d(n,t)$ accounts for the deterministic *growth rate* of the n-sized cluster, whereas the term $1/2\left[g(n,t) + d(n,t)\right]$ describes the fluctuative changes in the cluster size n. A comprehensive overview of the theory of nucleation and precipitate growth can be found in [36].

The terms $g(n,t)$ and $d(n,t)$ can be solved by discussing the widely used [10, 37] Ham's law for the precipitation of iron [38]:

$$\frac{\partial}{\partial t} [\mathrm{Fe_i}] = -4\pi r_c N_{\mathrm{p}} D_{\mathrm{Fe}} \left([\mathrm{Fe_i}] - S_{\mathrm{Fe}} \right), \tag{42}$$

where $[\mathrm{Fe_i}]$ is the total density of iron in interstitial form, r_c is the capture radius of the precipitatates and N_p is the density of precipitates. There are two typical ways to utilize Ham's law [10]:

1. Assuming a constant precipitate size which corresponds to a constant capture radius r_c and allowing the density of precipitates to change, i.e., allowing new precipitates to nucleate and old ones to completely dissolve.
2. Assuming a constant precipitate density N_p and allowing the existing precipitates to grow and diminish leading up to a varying capture radius.

Ideally, under high supersaturation, Eq. (41) should be reduced to Ham's law, because Ham's law has been demonstrated to work well under high supersaturation, i.e. when $[\mathrm{Fe_i}] \gg S_\mathrm{Fe}$ [37, 39]. Under high supersaturation, it can be assumed that the fluctuative changes are small compared to the deterministic changes and Eq. (41) can be simplfi-ied:

$$\frac{\partial}{\partial t} f(n,t) \approx \frac{\partial}{\partial n} \left\{ - \left[g(n,t) - d(n,t) \right] f(n,t) \right\}. \tag{43}$$

To reach a form which is comparable to the Ham's law, Eq. (43) is further manipulated. If Eq. (43) is multiplied by n and integrated over n the following equation is obtained:

$$\frac{\partial}{\partial t} [\mathrm{Fe}]_{\mathrm{FeSi_2}} = \int_1^M n \cdot \frac{\partial}{\partial n} \left\{ - \left[g(n,t) - d(n,t) \right] f(n,t) \right\} \mathrm{d}n. \tag{44}$$

Next, the following integrals for the total concentration of iron in precipitates $[\mathrm{Fe}]_{\mathrm{FeSi_2}}$ and the total concentration of precipitates N_p are necessary:

$$\int_1^M n f(n,t) \mathrm{d}n = [\mathrm{Fe}]_{\mathrm{FeSi_2}}, \tag{45}$$

$$\int_1^M f(n,t) \mathrm{d}n = N_\mathrm{p}. \tag{46}$$

Now, integrating by parts and using Eqs. (45) and (46), the right part of Eq. (44) can be

further manipulated:

$$\int_1^M n \cdot \frac{\partial}{\partial n}\{-[g(n,t) - d(n,t)]\, f(n,t)\}\, \mathrm{d}n =$$
$$\Big|_1^M \{-n \cdot [g(n,t) - d(n,t)]\, f(n,t)\} + \int_1^M [g(n,t) - d(n,t)]\, f(n,t)\mathrm{d}n = \tag{47}$$
$$\approx [g(n,t) - d(n,t)] \int_1^M f(n,t)\mathrm{d}n = [g(t) - d(t)]\, N_{\mathrm{p}}$$

In Eq. (47), it was assumed that the terms $f(1,t)$ and $f(M,t)$ are small compared to the total density of precipitates and the evaluation term of the integral can be ignored. Additionally, $g(n,t)$ and $d(n,t)$ were assumed to be independent of n. Noting that

$$\frac{\partial}{\partial t}[\mathrm{Fe_i}] = -\frac{\partial}{\partial t}[\mathrm{Fe}]_{\mathrm{FeSi_2}} \tag{48}$$

and combining Eqs. (44), (47) and (48) yields the following equation:

$$\frac{\partial}{\partial t}[\mathrm{Fe_i}] = -[g(t) - d(t)]\, N_{\mathrm{p}}. \tag{49}$$

In order for the approximated FPE to match Ham's law (Eqs. (42) and (49) , respectively), $g(n,t)$ and $d(n,t)$ are assigned as:

$$g(n,t) = 4\pi r_c(n) D_{\mathrm{Fe}}[\mathrm{Fe_i}], \text{ and } d(n,t) = 4\pi r_c(n) D_{\mathrm{Fe}} S_{\mathrm{Fe}}^n(n), \tag{50}$$

where $r_c(n)$ is the size dependent capture radius of iron precipitates and S_{Fe}^n is the size dependent equilibrium concentration of interstitial iron which matches S_{Fe} at the surface of a very large iron precipitate. This correlation is necessary because the solid solubility limit is measured under such conditions, under which the precipitates are expected to be large [6, 7]. However, S_{Fe}^n can generally be allowed to differ from S_{Fe} in order to take into account the size dependancy of the equilibrium concentration. The solute concentration at equilibrium with a precipitate of size n is the concentration, for which the change in Gibbs free energy ΔG vanishes, i.e. the solution for equation:

$$\frac{\partial}{\partial n}\Delta G\,[S_{\mathrm{Fe}}^n(n)] = 0, \tag{51}$$

where ΔG is the Gibbs free energy. Assuming that the thickness of the precipitate stays nearly constant, ΔG is given by [40]:

$$\Delta G(n) = -nk_{\mathrm{B}}T \ln\left(\frac{S^{n}_{\mathrm{Fe}}}{S_{\mathrm{Fe}}}\right) + 2E_{\mathrm{a}}n^{1/2}, \tag{52}$$

where E_{a} is a parameter consisting of the surface energy of the iron precipitate and the strain caused by the precipitate [40]. With Eqs. (51) and (52), the equilibrium concentration is readily obtained:

$$S^{n}_{\mathrm{Fe}}(n) = S_{\mathrm{Fe}} \exp\left(\frac{E_{\mathrm{a}}}{k_{\mathrm{B}}Tn^{1/2}}\right). \tag{53}$$

From Eq. (53) it is easily seen, that when the precipitates are large and $n \gg 1$, we have $S^{n}_{Fe}(n) \approx S_{Fe}$, which was the prerequisite for the size dependent solubility dictated by Ham's law. Lastly, the size-dependancy of $r_c(n)$ in Eq. (50) is assumed to be similar as in boron implanted emitters [41]:

$$r_c(n) = r_0 + 5.1 \cdot 10^{-9}\mathrm{cm}\,\sqrt{n}, \tag{54}$$

where r_0 is the capture radius of the precipitation site. Eq. (54) is the theoretical capture radius of a 5 nm thick disk-shaped precipitate [40] combined with a constant capture radius to account for the precipitatation *site* as well.

2.6 Structure and computational aspects of the simulator

The structure of the simulator is illustrated in Fig. 1. The inputs of the simulator are:

1. Interstitial iron concentration and distribution ($[\mathrm{Fe_i}]$). A typical simulation begins from high temperatures (for example by simulating the cooling of the silicon ingot) and thus all the iron is assumed to be homogeneously distributed within the wafer.
2. Precipitation site concentration and distribution (N_{site}).
3. Precipitated iron concentration at the precipitation sites ($[\mathrm{Fe}]_{\mathrm{FeSi_2}}$). If the simulation begins from a high temperature, precipitated iron concentration is set to zero.
4. The time-temperature profile of the wafer process to be simulated.

In addition to time-temperature profiles, the simulator can also simulate additional processing steps like emitter in-diffusion or surface etching.

After the inputs are given, the simulator begins to simulate the given time-temperature profile. At the beginning of each time step, the solubility and diffusivity of iron is set corresponding to the current temperature. If high concentrations of dopants are present (for example boron or phosphorus), their changes to the diffusivity and solubility are

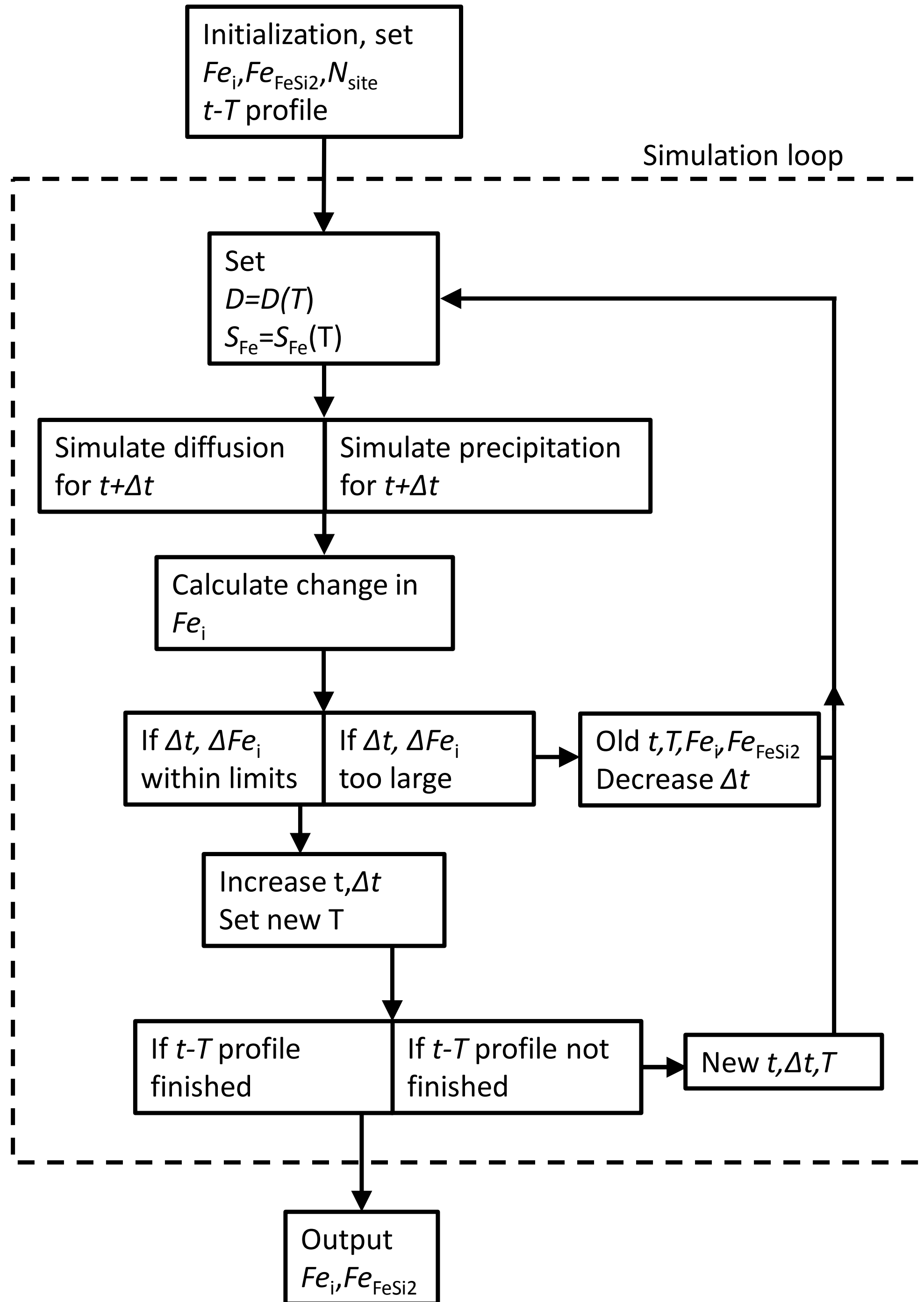

Figure 1: *A schematic of the computational structure of the simulator.*

accounted for as well. Then, the diffusion and precipitation of iron are simulated. The diffusion is calculated based on the equation introduced by Tan *et al.* and slightly modified by Hieslmair *et al.* to yield [42, 43]:

$$\frac{\partial}{\partial t}[\mathrm{Fe_i}] = \frac{\partial}{\partial x} J_{\mathrm{eff}}, \tag{55}$$

where J_{eff} is the effective iron flux, which accounts for varying solubility and diffusivity:

$$J_{\text{eff}} = -D_{\text{Fe}} S_{\text{Fe}}^{\max} \frac{\partial}{\partial x} \left(\frac{[\text{Fe}_\text{i}]}{S_{\text{Fe}}} \right), \tag{56}$$

where $S_{\text{Fe}}^{\max}$ is an operator, which chooses at each time step the maximum solubility of each neighboring node pair in the simulation grid. With the help of this operator, Eqs. (55) and (56) predict the magnitude of the flux correctly independent of the direction of the segregation [43].

Eq. (55) is differenced with the finite differences method and solved using the modified Crout's method presented in [43]. If a two dimensional simulation is simulated, the diffusion equation is at each time step first solved in the x-direction and then in the y-direction.

After simulating one time-iteration of the diffusion equation, one time-iteration of precipitation is simulated by solving the FPE (Eq. (41)). The FPE is differenced using the scheme of Chang and Cooper [44] and solved with the same modified Crout's method as the diffusion equation. After the new iron precipitate size distribution $f(n)$ is calculated, the new concentration of precipitated iron is calculated by:

$$[\text{Fe}]_{\text{FeSi}_2}^{\text{new}} = \int_1^M n f(n) \text{d}n, \tag{57}$$

and the corresponding new interstitial iron concentration by:

$$[\text{Fe}_\text{i}]^{\text{new}} = [\text{Fe}_\text{i}]^{\text{old}} - \left([\text{Fe}]_{\text{FeSi}_2}^{\text{new}} - [\text{Fe}]_{\text{FeSi}_2}^{\text{old}} \right). \tag{58}$$

The difference methods for both the diffusion and the Fokker-Planck equation are unconditionally stable, meaning that they cannot result in negative dissolved or precipitated iron concentrations. This allows the use of larger time steps when the changes in the interstitial iron concentration are relatively small, which is typical towards the end of various wafer processes, when iron concentration is close to its equilibrium value. To exploit this, the maximum relative change in the interstitial iron concentration among all the simulation points is checked after every time step. If this change remains smaller than a certain number, the time step is moderately increased and on the other hand, if the change is too large, the time step is decreased. Typically in this work, a maximum relative change of 10 % is allowed and the time step is multiplied by a factor of 1.03 or 0.75 if the changes are below or above this set value.

In addition to this regulation of the time step, every time the calculation described by Eq. (58) is performed, it must be checked that the interstitial iron concentration remains positive at each simulation point. If it turns negative, the result of the current time step are

rejected and the time step is redone with a smaller time step, until such a time step value is found, which does not result in a negative iron concentration.

As to the boundary conditions of the diffusion and Fokker-Planck equation, no-flux boundary conditions are facilitated for the diffusion equation at the edges of the simulation grid. The boundary condition $f(1,t)$ of the FPE, on the other hand, is:

$$f(1,t) = p_1 f(0,t) \exp\left[\frac{-\Delta G(1)}{k_\mathrm{B}T}\right], \tag{59}$$

where p_1 is a fitting parameter and $f(0,t)$ is the density of empty precipitation sites:

$$f(0,t) = N_\mathrm{site} - \int_1^M f(n,t)\mathrm{d}n. \tag{60}$$

In physical terms, Eq. (59) describes nucleation: $f(0,t)$ accounts for the available precipitation sites and the term $p_1 \exp\left[\frac{-\Delta G(1)}{k_\mathrm{B}T}\right]$ determines thermodynamically, which fraction of these sites contain an iron atom, i.e. where nucleation occurs.

The other boundary condition of the FPE is then defined as:

$$f(M,t) = 0. \tag{61}$$

In an analytic calculation, Eq. (61) would correspond to the boundary condition at $n \to \infty$. Thus in simulations, M needs to be set so large, that there are practically no precipitates, which grow that large. Otherwise Eq. (61) may cause loss of particles. In the simulations performed in this work, $M = 10^{10}$ atoms. Another possible boundary condition would be a no-flux boundary condition at the high n boundary, which might allow for the use of smaller n-grid and possibly save calculation time.

2.7 Nucleation and precipitation parameters

The fitting parameters E_a and p_1 have a strong impact on the nucleation and precipitation kinetics predicted by the simulator through Eqs. (52) and (59). Thus, a rigorous assessment of these parameters is required. Previously, they were estimated based on gettering experiments performed on boron doped wafers with a resistivity of around 30 Ωcm and an oxygen content of 15 ppma [9]. The density of oxide precipitates at the wafers N_{ox} was measured to be $1 \cdot 10^{10}$ cm^{-3} using optical microscopy after a selective Wright etch step. The size of the oxide precipitates was measeured to be approximately 80 nm using transmission electron microscopy (TEM) yielding for the capture radius of the oxide precipitates $r_\mathrm{ox} = 40$ nm. It was assumed that iron would precipite only at the oxide precipitates which allowed setting $N_\mathrm{site} = N_\mathrm{ox}$ and $r_c = r_\mathrm{ox}$, eliminating the need for other simulation parameters and leaving E_a and p_1 as the only fitting parameters.

In [9], the fitting of E_a and p_1 was performed using solubilities measured by Aoki *et al.* at temperatures of 800-1000 °C [6] and then extrapolating solubility values below 800 °C from their data. However, Murphy *et al.* have recently measured slightly higher solubilities below 800 °C than this extrapolation would predict. To account for this, E_a and p_1 are re-fitted for this work based on the experimental data in [9] and taking into account the new solubility data measured by Murphy *et al*.

The gettering experiment proceeded followingly. The p-type samples were contaminated with a method described in [9] to three different initial iron levels: $5 \cdot 10^{12}$, $2 \cdot 10^{13}$ and $8 \cdot 10^{13}$ cm^{-3}. After the contamination, the wafers went through a 30 min dissolution step at the iron in-diffusion temperature followed by a 50 °C/min cool to a 30 min gettering anneal at a varying temperature between 200 and 800 °C. After the gettering anneal, the wafers were cooled at a rate of 100 °C/min to room temperature and the remaining interstitial iron concentration was measured by microwave detected photoconductive decay (μ-PCD).

The 30 min gettering anneals were then simulated with the iron simulator presented in this chapter by setting N_site and r_c to the measured values of $1 \cdot 10^{10}$ cm^{-3} and 40 nm, respectively. To estimate p_1 and E_a, p_1 was set to $1 \cdot 10^4$ and E_a was then fitted based on the change in interstitial iron in the samples during the gettering anneals using the method of least squares. The results are illustrated in Fig. 2. For temperatures over 700 °C, or 973.15 K, the same E_a was chosen as in [9], due to their use in various publications [32, 41, 45]. The resulting E_a has the following piecewise defined formula:

$$E_\mathrm{a} = \begin{cases} 1.952 \cdot 10^{-4} \cdot (T/\mathrm{K}) + 0.6816\ [\mathrm{eV}],\ T \leq 773.15\ \mathrm{K} \\ 6.038 \cdot 10^{-4} \cdot (T/\mathrm{K}) + 0.415\ [\mathrm{eV}],\ 773.15\ \mathrm{K} < T \leq 973.15\ \mathrm{K} \\ 8.408 \cdot 10^{-4} \cdot (T/\mathrm{K}) + 0.1843\ [\mathrm{eV}],\ T > 973.15\ \mathrm{K}. \end{cases} \tag{62}$$

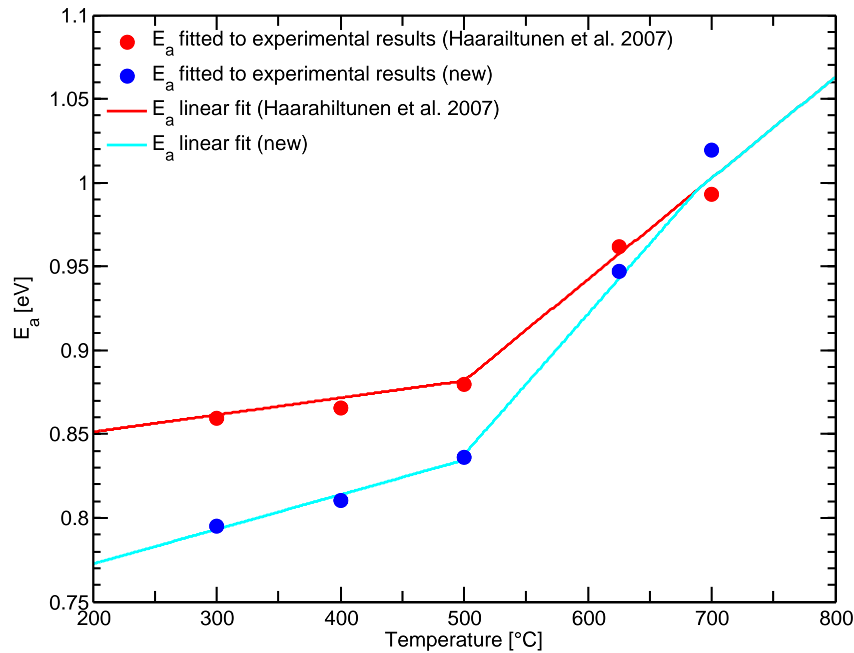

(a) *The newly fitted E_a compared to that calculated in [9].*

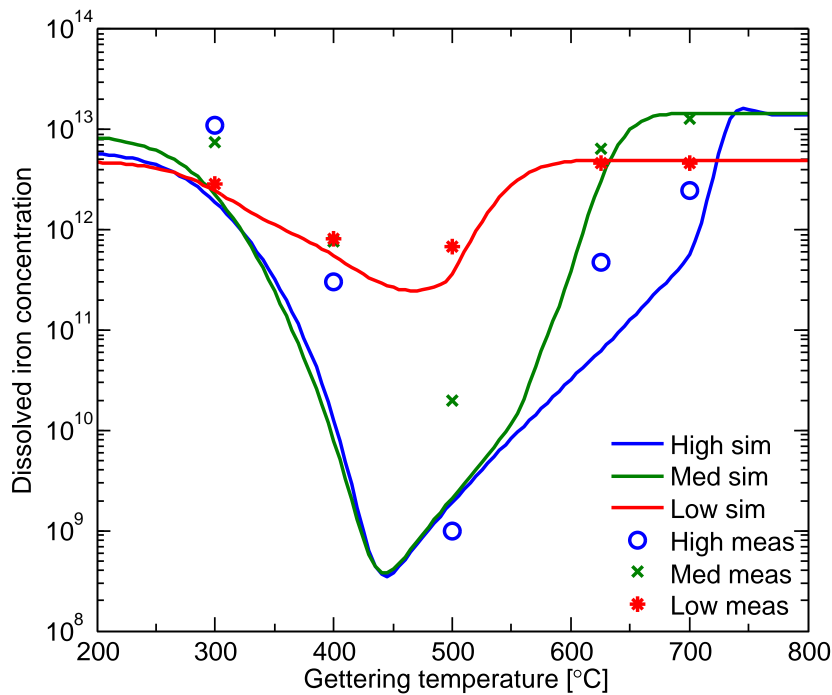

(b) *Simulations based on the new E_a.*

Figure 2: *a) The results of the least square fit for E_a compared to the previous E_a calculated in [9]. The differences are caused by the different solubility values used in the calculations. b) Simulation results based on the new E_a compared to the experimental results of the gettering anneals done in [9]. The slight discrepancy between the measured and simulated values are caused by the fact that when fitting E_a, the ramps before and after the isothermal gettering anneal were not taken into account.*

3 Experimental methods used to study iron in silicon wafers

To quantitatively study the gettering efficiency of different wafer processess, methods to measure the distribution of both interstitial and precipitated iron in silicon wafers are necessary. This section present two such tools which are used in this work. Surface photovoltage method (SPV) is used to study the interstitial iron concentration in the bulk of the wafers, and synchrotron-based micro-X-ray fluorescence (μ-XRF) is used to probe the distribution of precipitated iron at the emitter.

3.1 Quantifying the interstitial iron concentration by the surface photovoltage method

Surface photovoltage is a convenient tool for measuring the interstitial iron concentration in silicon wafers down to concentrations of $10^9 - 10^{11}$ cm^{-3}, depending on the material quality and the sensitivity of the instrumentation [46]. SPV is widely used because it is non-destructive and contactless, it does not require laborious sample preparation and it is a steady-state method, which makes it relatively immune to the slow trapping and detrapping effects that can influence transient measurements. This section briefly summarizes the operational and physical principles of the SPV technique.

3.1.1 Measurement setup in the SPV method

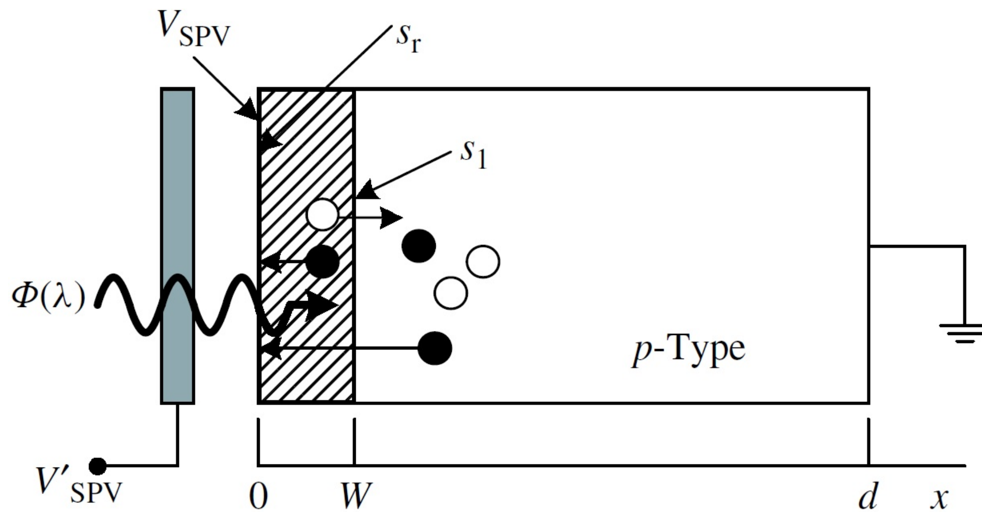

Figure 3: *A schematic of the SPV measurement setup. $\Phi(\lambda)$ is the wavelength dependent photon flux density of the incoming light, V_{SPV} the induced voltage, s_r the surface recombination velocity at the front surface of the sample, s_1 the surface recombination velocity at the edge of the scr, W the width of the scr and d the sample thickness. Reproduced with permission from [47].*

A space-charge region (scr) is induced near the sample surface by for example a corona charge. The other surface is kept in the dark and the surface with the induced scr is uniformly illuminated by monochromatic light of energy higher than the sample band gap. The light creates electron-hole pairs within the sample and some of the generated minority carriers diffuse toward the illuminated surface and are collected by the space-charge region establishing a surface potential or surface photovoltage voltage relative to the grounded back surface. The measurement setup is illustrated in Fig. 3.

3.1.2 Gauging the minority carrier diffusion length

This section determines the relationship between the minority carrier diffusion length D_L in the sample and the induced surface photovoltage voltage V_{SPV}. First, a diffusion length dependent expression for the excess minority carrier density at the scr edge is determined. Then, a relationship between the induced voltage and the excess minority carrier is presented resulting in a relationship between the diffusion length and the induced voltage. Throughout this section, a p-type doping in the bulk is assumed, but the same equations hold correspondingly also for n-type doping.

When determining the diffusion length dependent expression for the excess minority carrier density, following assumptions are made:

1. The scr width is small compared to the sample thickness and the absorption coefficient of the wafer $\alpha(\lambda)$ is large enough, that the majority of the incoming photons are absorbed in the bulk of the wafer.
2. The wafer thickness should be much larger than the minority carrier diffusion length.
3. The light intensity should be low enough for low-level injection conditions to prevail.
4. The light diameter should be large compared to the sample thickness to allow a one-dimensional analysis.

Assumptions 1-3 can be expressed as equations:

$$d - W \geq 4D_L;\ W \ll D_L;\ \alpha W \ll 1;\ \alpha(d - W) \gg 1;\ \Delta n \ll p_0, \tag{63}$$

where p_0 is the equilibrium hole density. Assuming a p-type doping, the one-dimensional continuity equation for the excess minority carrier density $\Delta n(x)$ throughout the sample is:

$$D_n \frac{d^2 \Delta n(x)}{dx^2} - \frac{\Delta n(x)}{\tau_n} + G(x) = 0, \tag{64}$$

where D_n is the minority carrier diffusivity, τ_n the minority carrier lifetime and G the minority carrier generation rate, which is defined as a function of incoming photon flux

density Φ and the reflectivity of the front surface R:

$$G(x,\lambda) = \Phi(\lambda)\alpha(\lambda)\,[1 - R(\lambda)]\exp(\alpha x)\,. \tag{65}$$

In Eq. (65), it is assumed that each photon creates an electron hole pair. If the surface recombination velocity at the back surface of the sample is s_{r2} and the following boundary conditions for the continuity equation are assumed:

$$\left.\frac{d\Delta n(x)}{dx}\right|_{x=0} = s_r\frac{\Delta n(0)}{D_n} \text{ and } \left.\frac{d\Delta n(x)}{dx}\right|_{x=d} = -s_{r2}\frac{\Delta n(d)}{D_n}, \tag{66}$$

with the help of assumptions (64), a following expression for the excess minority carrier density at the edge of the scr can be obtained [47]:

$$\Delta n(W) \approx \frac{(1-R)\Phi}{(s_1 + D_n/D_L)}\frac{\alpha D_L}{(1+\alpha D_L)}. \tag{67}$$

The induced voltage is caused solely by the excess minority carriers at the edge of the scr. Thus, $\Delta n(W)$ is related to the voltage through the diode equation:

$$\Delta n(W) = n_{po}\left(\exp\left(\frac{qV_{\mathrm{SPV}}}{k_{\mathrm{B}}T}\right) - 1\right) \approx n_{po}\frac{qV_{\mathrm{SPV}}}{k_{\mathrm{B}}T}, \text{ for } V_{\mathrm{SPV}} \ll \frac{k_{\mathrm{B}}T}{q}, \tag{68}$$

where n_{po} is the equilibrium electron density in the p-doped wafer. Now, the combination of Eqs. (67) and (68) results in:

$$V_{\mathrm{SPV}} = \frac{(k_{\mathrm{B}}T/q)(1-R)\Phi D_L}{n_{po}(s_1 + D_n/D_L)(D_L + 1/\alpha)}. \tag{69}$$

During SPV measurements, the surface photovoltage V_{SPV} is directly measured, whereas the photon flux density Φ and the wavelength of the photons can be freely adjusted. This results in two possible ways to determine the minority carrier diffusion length D_L. In both implementations, the wavelength of the photons is varied to give different absorption coefficients α. The varying absorption coefficient results in different excess minority carrier densities at the edge of the scr. In the first implementation, the change caused by the different wavelength is compensated by adjusting the photon flux density such that the *surface photovoltage remains constant*. Then, plotting Φ againt $1/\alpha$ gives D_L, as can be seen by rewriting Eq. (69) as:

$$\Phi = V_{\mathrm{SPV}}\frac{n_{po}(s_1 + D_n/D_L)(D_L + 1/\alpha)}{(k_{\mathrm{B}}T/q)(1-R)D_L} \equiv C_1\left(D_L + \frac{1}{\alpha}\right), \tag{70}$$

where C_1 is a constant.

In the other implementation, the *photon flux density is kept constant*, and V_{SPV} is plotted against α. Then Eq. (69) should be rewritten as:

$$\frac{1}{V_{\mathrm{SPV}}} = \frac{n_{po}(s_1 + D_n/D_L)(D_L + 1/\alpha)}{(k_{\mathrm{B}}T/q)(1-R)D_L\Phi} \equiv C_2\left(D_L + \frac{1}{\alpha}\right), \tag{71}$$

where C_2 is a constant.

3.1.3 Determining the interstitial iron concentration

Due to the tendency of iron to form $\mathrm{Fe_iB}$ pairs when boron is present (as explained in section 2.3), it is possible to utilize SPV to measure interstitial iron concentration in p-type silicon wafers. Eq. (22) predicts that in room temperature with doping levels of $[\mathrm{B}] > 10^{14}\ \mathrm{cm^{-3}}$, most of the iron is paired with boron. However, the $\mathrm{Fe_iB}$ pairs can easily be dissociated into interstitial iron and subsitutional boron by a short heat treatment, for example 10 minutes of annealing at 200 °C, or by strong light impulses. Because the trap level of the $\mathrm{Fe_iB}$ pair is more shallow than the trap level of the interstitial iron (0.1 eV+E_{V} compared to 0.4 eV+E_{V}), the diffusion length decreases considerably when the $\mathrm{Fe_iB}$ pairs are dissociated [48]. If the diffusion length is measured before and after the dissociation of the $\mathrm{Fe_iB}$ pairs, the interstitial iron concentration can be calculated with the formula [48]:

$$[\mathrm{Fe_i}] = \frac{D_n}{f_{\mathrm{diss}}}\left(\frac{1}{L_1^2} - \frac{1}{L_0^2}\right)\Bigg/\left(C_n\left(\mathrm{Fe_i}\right) - \frac{C_n\left(\mathrm{Fe_iB}\right)}{\exp\left[\left(E_{\mathrm{F}} - 0.1\ \mathrm{eV}\right)/k_{\mathrm{B}}T\right]}\right), \tag{72}$$

where L_0 and L_1 are the measured diffusion lengths before and after the dissociation of iron boron pairs, respectively, f_{diss} is the fraction of dissociated boron pairs and $C_n\left(\mathrm{Fe_i}\right)$ and $C_n\left(\mathrm{Fe_iB}\right)$ are the electron capture coefficients for interstitial iron and iron boron pairs, respectively. Because of the uncertainty in the electron capture coefficients and the fraction of iron boron pairs dissociated, in practice the relationship between the interstitial iron concentration and the change in the diffusion length is measured with the empirical equation:

$$[\mathrm{Fe_i}] = C_{\mathrm{SPV}}\left(\frac{1}{L_1^2} - \frac{1}{L_0^2}\right), \tag{73}$$

where C_{SPV} is a calibration constant. In this work, a piecewise defined calibration constant based on experimental data is used [49, 50]:

$$C_{\mathrm{SPV}} = \begin{cases} 3.55\cdot 10^{15}\ \frac{\mu\mathrm{m}^2}{\mathrm{cm}^3}, & \left(\frac{1}{L_1^2} - \frac{1}{L_0^2}\right) \geq 1\cdot 10^{-3}\mu\mathrm{m}^{-2}, \\ 7.80\cdot 10^{15}\ \frac{\mu\mathrm{m}^2}{\mathrm{cm}^3}, & \left(\frac{1}{L_1^2} - \frac{1}{L_0^2}\right) < 1\cdot 10^{-3}\mu\mathrm{m}^{-2}. \end{cases} \tag{74}$$

3.2 Quantifying the distribution of iron precipitates by synchrotron-based micro-X-ray fluorescence

While obtaining information of the homogeneously scattered interstitial iron distribution in silicon wafers is relatively simple, studying the iron precipitates on a quantitative level is more challenging. The precipitates are relatively small and sparsely scattered, typically ranging less than a hundred nanometer with a density lower than 10^9 cm^{-3} [51, 52]. Thus they are difficult to observe by for example transmission electron microscopy (TEM) due to its low sampling volume and destructive sample preparation or by electron beam induced current (EBIC) due to its relatively low spatial resolution of a couple of micrometers [53]. In this work, iron precipitates in silicon wafers are probed by synchrotron-based micro-X-ray fluorescence.

The µ-XRF measurements performed in this work were performed at beamline 2-ID-D at the Advanced Photon Source of Argonne National Laboratory in Illinois, US [54]. The beamline is capable of measuring hundreds of µm^2 with a 220 nm step size.

3.2.1 X-ray fluorescence as an electronic process

The atomic level electronic processes involved in the µ-XRF technique are described in Fig. 4. The probed atoms absorb the incident X-rays by emitting electrons from the atomic K-shell. The hole in the deep K-shell is then replaced by an electron from a higher lying level, for example the L-shell. The energy liberated in the latter process is released as X-rays. This particular transition is called the $K\alpha$ transition. Other transitions are of course possible, but the $K\alpha$ transition is the most dominant one and is thus utilized in the µ-XRF technique.

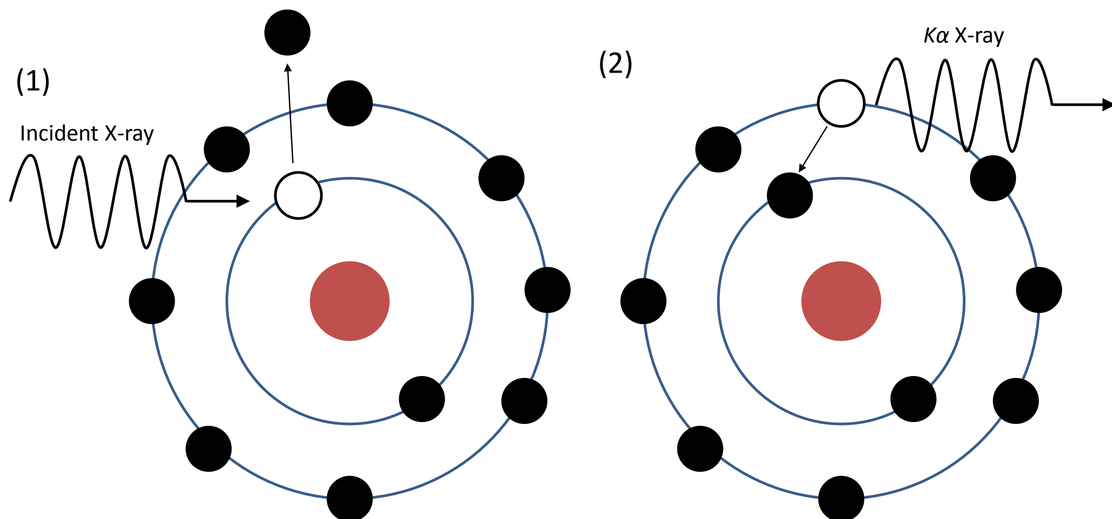

Figure 4: *X-ray fluorescence as an electronic process.*

The $K\alpha$ transition energy is characteristic for each element. Thus, different elements can be distinguished by observing different energy regions. Also, the energy of the incident X-rays have to be larger than the energy required to excite the electron from the K-shell, i.e. the K-edge of the impurity species in question. For iron, the K-edge is 7.11 keV [55] and the $K\alpha_{1,2}$ transition energies approximately 6.40 keV [56]. In Fig. 5, there is an example of a photon energy spectrum collected from a spot on an iron contaminated silicon sample hit by a 10 keV incident photon beam. In addition to the iron $K\alpha$ peak, similar peaks caused by copper, zinc and silicon are recognized. Because of the finite deadtime of the detector, all the Si $K\alpha$ X-rays cannot be distinguished resulting in a secondary Si $K\alpha$ peak.

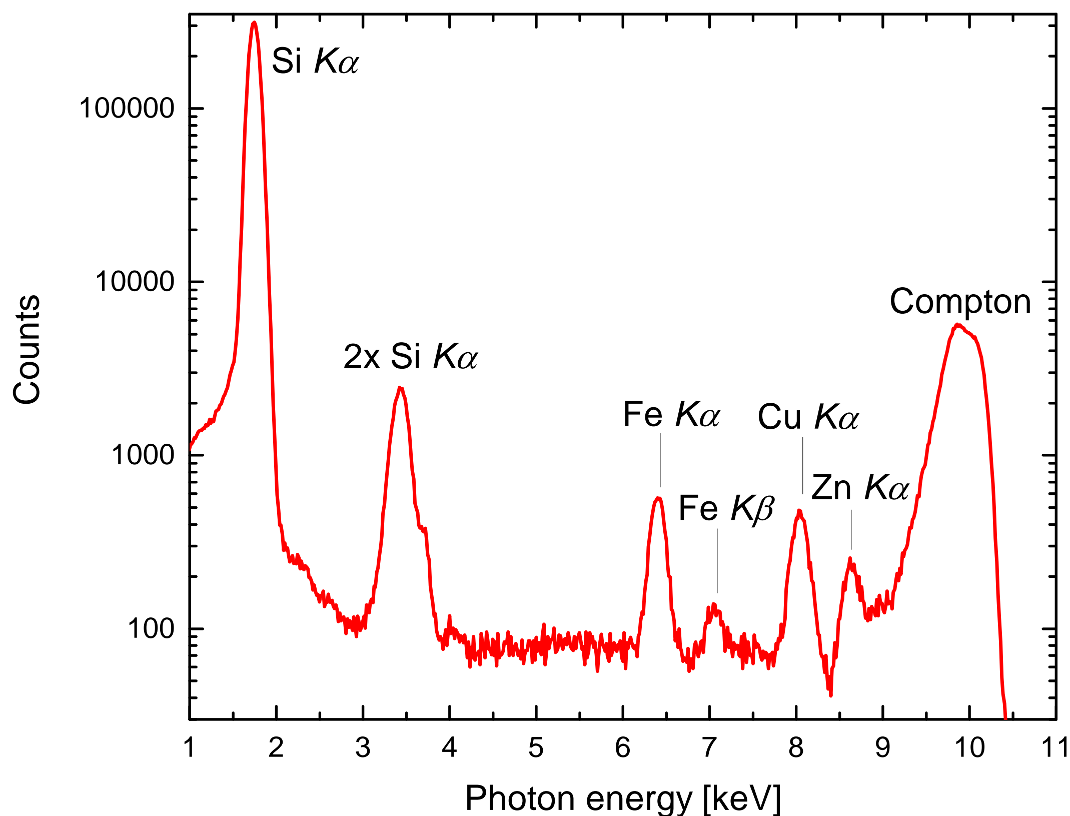

Figure 5: *A typical energy spectrum collected from a spot on an iron contaminated silicon sample with μ-XRF. In addition to iron, also copper and zinc are recognized.*

3.2.2 Measurement setup and information depth of the μ-XRF technique

The measurement geometry used in the μ-XRF measurements of this work is illustrated in Fig. 6. The sample is placed on a nanopositioning stage, which allows high xy-resolution. The X-rays of the incident beam and the emitted $K\alpha$ X-rays are absorbed in the material according to the equation:

$$I(x) = I_0 \exp\left[-(\mu/\rho)\,\rho\right], \tag{75}$$

where $I(x)$ is the depth dependent intensity of the X-ray beam, I_0 the intensity of the original beam, μ/ρ the (energy dependent) mass absorption coefficient of the probed material and ρ the material density. The effective information depth d_{inf} of the measurement setup is defined as:

$$\frac{1}{d_{\text{inf}}} = \frac{1}{d_1} + \frac{1}{d_2}, \tag{76}$$

where d_1 is the 1/e attenuation length of the incident beam and d_2 the 1/e attenuation length of the secondary beam. Using the mass absorption coefficients of silicon from [57] and Eqs. (75) and (76), the effective information depth with the measurement geomtery depicted in Fig. 6 with a 10 keV incident beam can be calculated to be 8.8 μm.

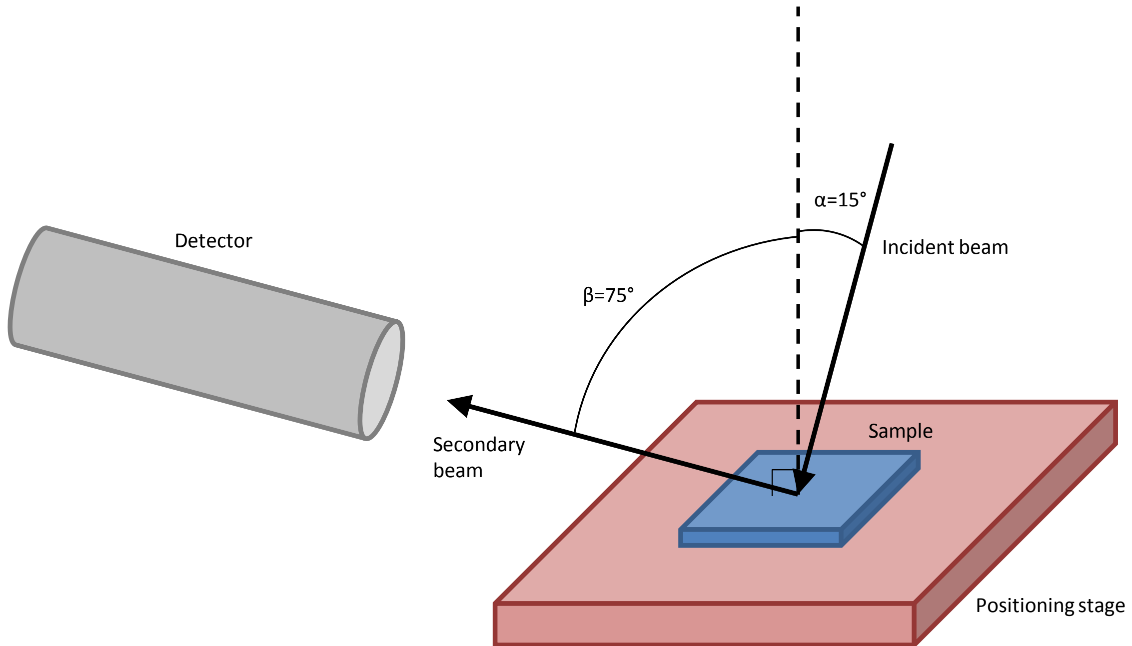

Figure 6: *Measurement geometry of* μ*-XRF.*

3.2.3 Discerning iron precipitates from μ-XRF data maps

Once the X-ray fluorescence spectrum is gathered from each measured pixel, the fluorescence counts are transformed into iron loadings [μg/cm^2] by comparing the fluorescence counts to NIST 1832 and 1833 standards with the help of the peak fitting method suggested by Vogt *et al.* [58]. The Fe loading value can be converted from μg/cm^2 to atoms (per pixel) with the formula:

$$N_{\mathrm{atoms}} = L_{\mathrm{Fe}} \left(\frac{\pi D^2}{4} \right) \frac{N_{\mathrm{A}}}{M_{\mathrm{Fe}}}, \tag{77}$$

where L_{Fe} is the iron loading in μg/cm^2, D the full-width half maximum (FWHM) diameter of the incident beam in cm, N_{A} Avogadro's constant and M_{Fe} the molar mass of Fe in μg/mol.

Next, the actual iron precipitate signals need to be distinguished from the noise. Thus, the loadings from each pixel on a single data map are fitted on a truncated Gaussian distribution. A truncated normal distribution is assumed because of the physical impossiblity of measuring iron counts in the detector system below. The distribution is also truncated from the right to distinguish the high Fe pixels including real precipitates from the statistical noise. For this work, the higher truncation point was chosen to be twice the most common Fe loading value, when the loading values from the pixels were divided into 100 bins. After this, the mean μ and standard deviation σ of the truncated Gaussian distribution are estimated with the maximum likelihood method.

After estimating μ and σ, all pixels with readings below $\mu + 3.5\sigma$ are assumed noise, as was done in [51]. After this, individual precipitates are detected from the data maps using a MATLAB image processing algorithm, *bwconncomp* using a connectivity of four. The method counts each pixel pair which share an edge as belonging to the same precipitate. Then the total iron in each precipitate is counted by summing over all the pixels of each precipitate. This method may exaggerate the precipitate sizes, as high-Fe pixels may bleed into neighboring pixels.

4 Wafer treatments studied in this work

4.1 Sample preparation and gettering anneals

The samples studied in this work were 400 μm thick, monocrystalline p-type wafers with a resistivity of 2.7-3.0 Ωcm and a low initial oxygen level (7-9 ppma). These samples were intentionally contaminated with a method described in [17] to two different iron levels: 1) $1 \cdot 10^{13}$ cm^{-3} (medium) and 2) $2 \cdot 10^{14}$ cm^{-3} (high). After contamination, a thin screen oxide was grown on the wafers and a phosphorus dose of 10^{15} cm^{-2} with an energy of 50 keV was implanted on one side of the wafers to form an emitter. The wafers were annealed at 1000 °C for 40 min to activate the implant. After activation, the samples were cooled down at 2-4 °C/min for a gettering anneal at i) 800 °C for 2 h, ii) 750 °C for 3.5 h, iii) 620 °C for 8 h or iv) quenched to room temperature (RT) from 895 °C and then inserted back to furnace for an 8 h anneal at 620 °C (see Fig. 7). The samples will subsequently be referred to according to the temperature of their gettering anneals. The sample, on which the room temperature pullout was performed, will be referred to as the "RT+620 °C" sample. After the gettering anneals, the interstitial iron concentration was measured with SPV from all the samples. Further sample preparation can be found elsewhere [5].

Following supplementary experiments were performed in order to gauge the gettering procedure in more detail. In the first experiment, a group of wafers were processed identically as the RT+620 °C wafers, but they were left without the P implantation. In the second experiment, the mediumly and highly contaminated samples from both the implanted and intrinsic RT+620 °C wafers went through an etching treatment in a CH_3COOH:HF:HNO_3 solution. This treatment was estimated to etch away 23 μm of both the back and the front surfaces. After etching, the wafers underwent a dissolution anneal of 20 min at 1000 °C, which is higher than the iron in-diffusion temperature. The interstitial iron concentration was measured with SPV from the supplementary samples before and after the dissolution anneal. Lastly, also a reference cell without any contamination or a gettering anneal was processed. As a summary, all the studied treatments are collected in Tab. 3.

Table 3: *Wafer treatments studied in this work. All the contaminated processes were studied with a high iron concentration sample ($2 \cdot 10^{14}$ cm^{-3}) and medium iron concentration sample ($1 \cdot 10^{13}$ cm^{-3}). Also, all the implanted samples underwent a 1000 °C activation anneal for 40 min to activate the implant and to reduce implantation damage.*

Contamination	Implantation dose and energy	Gettering annal	Dissolution anneal
Yes	10^{15} cm^{-2}, 50 keV	2 h at 800 °C	None
Yes	10^{15} cm^{-2}, 50 keV	3.5 h at 750 °C	None
Yes	10^{15} cm^{-2}, 50 keV	8 h at 620 °C	None
Yes	10^{15} cm^{-2}, 50 keV	RT pullout + 8 h at 620 °C	None
Yes	10^{15} cm^{-2}, 50 keV	RT pullout + 8 h at 620 °C	20 min at 1000 °C
Yes	None	RT pullout + 8h at 620 °C	None
Yes	None	RT pullout + 8h at 620 °C	20 min at 1000 °C
No	10^{15} cm^{-2}, 50 keV	None	None

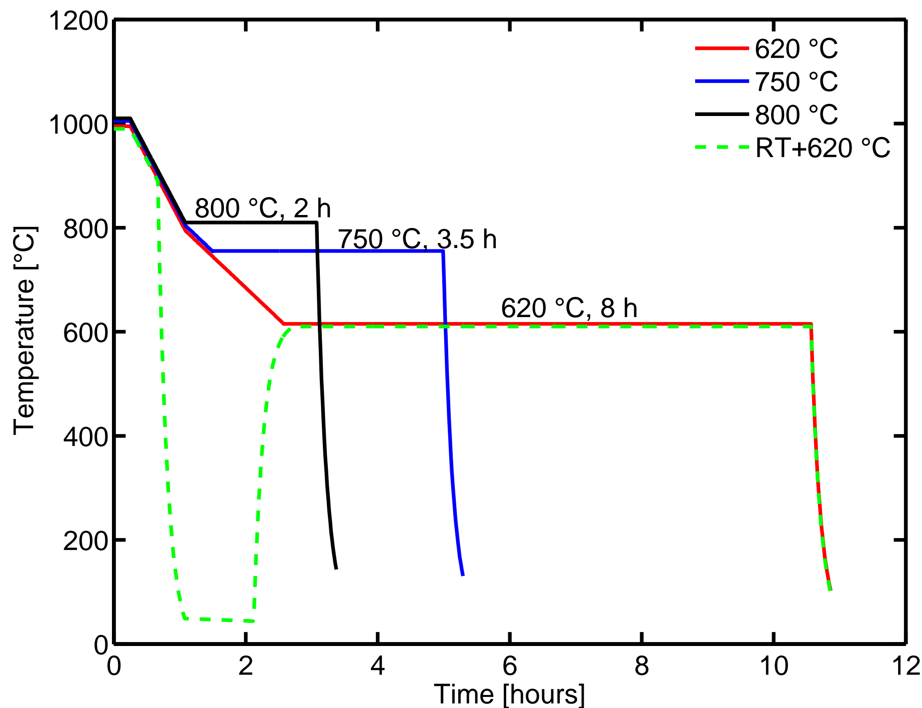

Figure 7: *Gettering anneals studied in this work. The linear ramp rates before the isothermal gettering anneal are 4 °C/min at temperatures over 800 °C and 2 °C/min at temperatures below 800 °C. The length and temperature of the isothermal gettering anneal are shown. Two samples underwent the 620 °C isothermal anneal. One was ramped slowly to the gettering anneal, and the other was slowly cooled to 895 °C, then pulled out at the oven to room temperature and subsequently reheated to 620 ° C for the 8 h gettering anneal. After the isothermal anneals, all the samples were directly pulled out from the furnace, experiencing a rapid cool down.*

4.2 Preliminary experimental findings: importance of precipitation

The gettering efficiency, i.e. the reduction in interstitial iron concentration caused by the gettering anneals described in Section 4.1 has been reported earlier [5]. The results are analyzed in detail in Section 5.3, but a few of the most central observations presented in [5] are repeated here:

1. For all the gettering anneals except the 800 °C anneal, a higher initial interstitial iron concentration leads to a lower interstitial iron concentration after processing.
2. Both the mediumly and highly contaminated RT+620 °C samples experienced a higher reduction of interstitial iron than the 620 °C samples.
3. The interstitial iron concentration is not reduced lower than the solid solubility of iron in any of the gettering temperatures.

All the observations listed above point to the fact, that the dominant gettering mechanism in the samples was precipitation. The higher initial iron concentration level causes a higher iron supersaturation, which leads to stronger nucleation during the ramp before the isothermal anneal, increasing the density of precipitates present during the isothermal anneal. During the isothermal anneal the precipitates ripen (grow) and the higher density of precipitates can internally getter iron to such extent that the effect of the initial, higher interstitial iron level is compensated. This explaines observation 1. In the model used in this work, the effect of the supersaturation on nucleation can be seen through the boundary-condition of the FPE, i.e. Eqs. (52) and (59).

Observation 2 is also interesting because the 620 °C sample is held at a higher temperature for a longer time than the RT+620 °C sample as is evident from Fig. 7. For example in the traditional phosphorus diffusion gettering, a higher temperature and longer time typically means better gettering efficiency [18]. However, similar to observation 1, observation 2 can also be understood by discussing nucleation during the ramp before the isothermal anneal. During the rapid cool down, the supersaturation of iron remains high but diffusivity relatively low, making nucleation preferential for individual iron atoms as opposed to transport to already existing precipitates. Thus, the rapid cool down leads to a high density of precipitates, which can correspondingly getter more iron during the isothermal anneal.

Observation 3 implies that segregation gettering is not strong enough to drive the iron concentration under the solid solubility limit in any of the samples. This suggests that if segregation does occur, its effect is relatively weak.

Further measurements of the highly contaminated 750 °C, 620 °C and RT+620 °C samples offered more evidence for the important role of precipitation. The minority carrier diffusion length in the bulk measured with SPV from the wafers after gettering [5] and the open circuit voltage measured from the solar cells made from the wafers are presented in Fig. 8. Even though the 620 °C and RT+620 °C samples differ only in the different ramp from the implantation anneal to the gettering anneal, their macroscopical propertier differ distinctly. In the 620 °C sample, the diffusion length is high whereas the open circuit

voltage V_{OC} is very low compared to that of the reference cell, which was not subjected to contamination or a gettering anneal after the implantation. On the contrary, in the RT+620 °C sample, the minority carrier diffusion length is low and the open circuit voltage close to that of the reference cell. Also in the 750 °C sample, the open circuit voltage is very low. These properties cannot be directly understood by discussing the interstitial iron concentration in the samples. Possible causes for this peculiar behavior are discussed in Section 5.

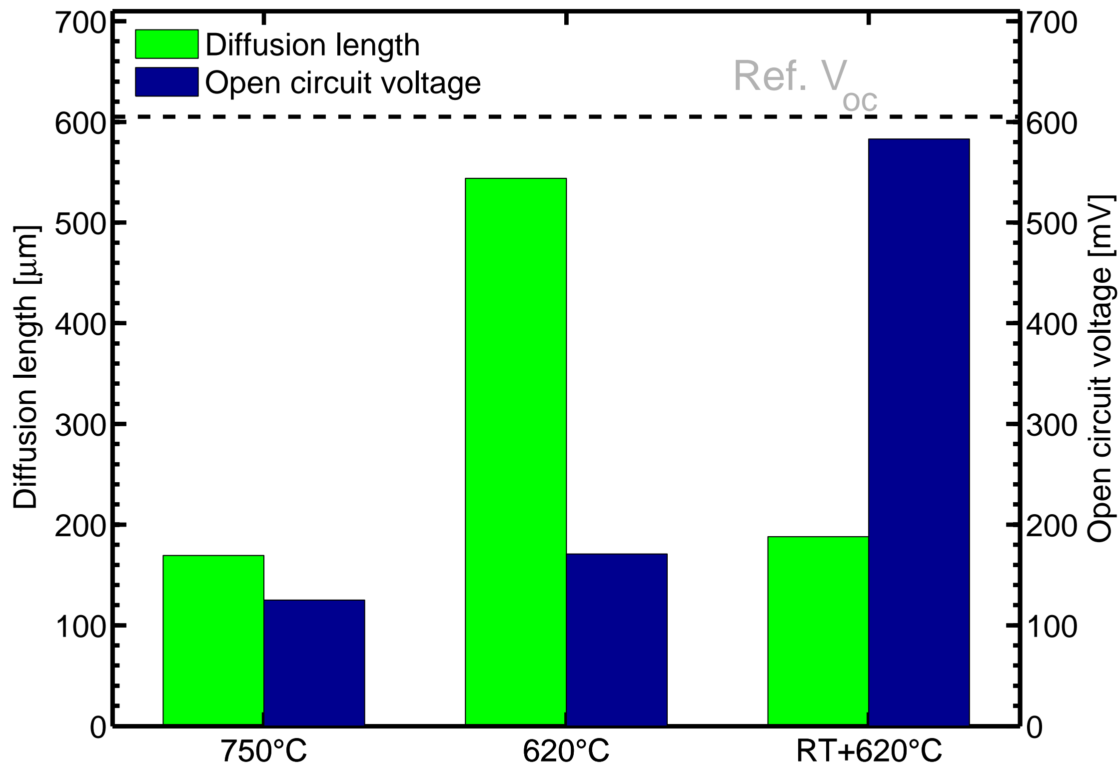

Figure 8: *The minority carrier diffusion length in the bulk measured with SPV after the gettering anneals as reported in [5] and the open circuit voltage measured from the solar cells made from the gettered wafers are shown for selected gettering anneals. The open circuit voltage measured from the uncontaminated reference cell is shown by the dashed line. The discrepancy of the diffusion length and the open circuit voltage between the 620 °C and RT+620 °C samples is peculiar.*

5 Simulation results

5.1 Hypothesis: Macroscopic effect caused by precipitate size distribution

The hypothesis of this work is that the abnormal discrepancy between the D_L and V_{OC} values in the 620 °C and RT+620 °C samples and the V_{OC} loss in the 750 °C sample illustrated in Fig. 8 can be explained by the different precipitate size distributions of the samples. As explained earlier, the RT+620 °C is likely to have a large density of precipitates, which could act as minority carrier recombination centers and lower the diffusion length [59]. On the other hand, in the 750 °C and 620 °C samples, the density of precipitates is lower and thus the same amount of iron is precipitated into fewer precipitates resulting in precipitates, which are larger in size. Theoretically, the precipitates at the emitter could grow large enough to short the junction, ruining the V_{OC}.

To verify this hypothesis, the precipitate size distributions in the 750 °C, 620 °C and RT+620 °C samples are studied in this section with the help of the iron simulator presented in section 2.

5.2 Density of precipitation sites in non-implanted silicon

In order to accurately estimate the precipitate size distributions, the gettering processes described in Section 4.1 were simulated using the simulation model described in Section 2. Before this could be done however, three simulation parameters needed to be fixed: i) the precipitation site capture radius r_0, ii) the density of precipitation sites N_{site} and iii) the segregation coefficient of the emitter. The precipitation was mostly expected to happen at the implantation damage caused by the emitter formation. Thus, a value of 5 nm was chosen for r_0 because a value of 15 nm has been used previously to model precipitation at bulk defects [45], where the defects are expected to be larger. It should be noted that this value acts merely as an estimate, but minor modifications to this value do not have a major impact on the simulation results. The density of precipitation sites in the bulk and at the silicon-oxide interface was estimated based on the etching and dissolution anneal tests performed earlier [5]. The following assumptions were made in the simulations:

1. The precipitation sites at the emitter or the silicon oxide-interface are located in the first 100 nm below the surface.
2. During the dissolution anneal, precipitated iron is fully dissolved.
3. The precipitation sites within the bulk are spread homogeneously.
4. The time temperature profile of the room temperature pull out is an exponential cool down with a time constant of 9 minutes.

The 100 nm value in assumption 1 is based on the secondary ion mass spectrometry (SIMS) measurements performed earlier [5], which indicated that after the implantation

and the gettering anneals, there was an anomalously high iron concentration in the first 100 nm below the surface. The same 100 nm value was chosen for the silicon-oxide interface for convenience. At the silicon-oxide interface the precipitation sites may be spread slightly differently, but the simulations should predict the *total* amount of precipitation sites correctly. The time constant of the exponential cool-down, on the other hand, was estimated to be 9 min, because earlier a 6 min time constant was used with a furnace, which ejected the wafers slightly faster than the furnace used in this study [60].

The estimation of the precipitation site densities in the bulk and at the silicon-oxide interface proceeded followingly. Based on the experimental results [5], most of the iron was assumed to precipitate at the silicon-oxide interface. Thus, the density of precipitation sites at the silicon-oxide interface was gauged first by placing no precipitation sites to the bulk. Then the density of precipitation sites at the silicon-oxide interfaces both at the front and at the backside of the wafer were set to the same value and an appropriate value resulting in more or less the experimentally observed gettering efficiency at the emitterless sample was obtained via simulations.

After reaching an estimate for the density at the silicon-oxide interface, the density of precipitation sites in the bulk was assessed. The density of precipitation sites in the bulk was increased while simultaneously the density of precipitation sites at the silicon-oxide interfaces was decreased in order to keep the total simulated gettering efficiency the same. The density in the bulk was increased until the simulations predicted a similar amount of iron precipitated in the bulk as was deduced from the dissolution experiments performed on the emitterless sample in [5].

After fixing the densities of the precipitation sites in the bulk and the silicon-oxide interface, the dissolution experiments performed for the RT+620 °C sample *with* the emitter were simulated with the emitter parameters justified in Section 5.3 for a final review and slight calibration of the parameters. The density parameters, which reproduced the experimental gettering efficiencies and the results of the dissolution tests optimally in simulations were $3.3 \cdot 10^5/\mathrm{cm}^3$ and $2 \cdot 10^{10}/\mathrm{cm}^3$ in the bulk and at the silicon-oxide interface, respectively.

The simulated results are compared to the experiments in Fig. 9. There is one interesting aspect, in which the experimental and simulated results differ. It seems that in the experiments, the amount of iron precipitated at the surfaces and in the bulk of the wafers are to a large extent similar both with and without the emitter, even though in the mediumly contaminated sample there is a distinct difference in the gettering efficiency with and without the emitter. This suggests that given a large enough supersaturation, the room temperature pullout causes such widespread nucleation that the exact properties of the emitter are insignificant. This kind of behavior is not predicted by the model used in this work and contributes to the slight discrepancy between the simulated and measured results in all the samples in Fig. 9.

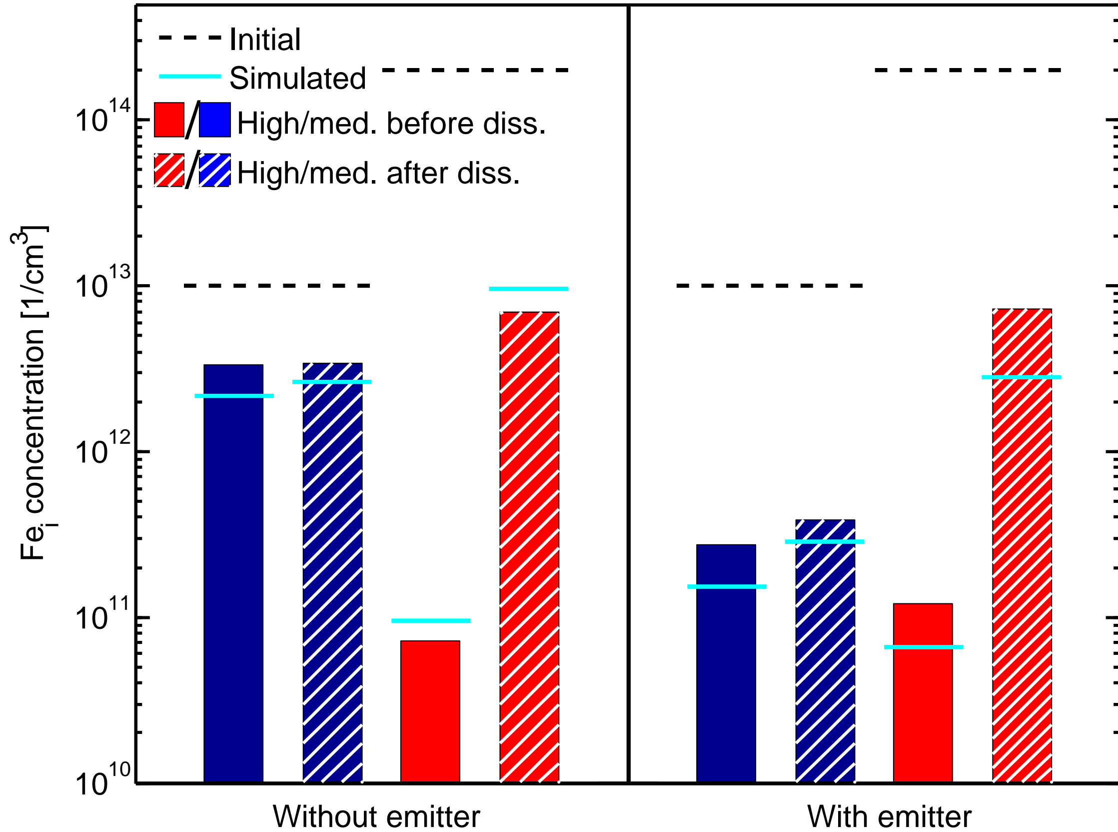

Figure 9: *Experimental results from previous dissolution tests made for the RT+620 °C sample [5] compared to simulation results. The blue and red bars depict the interstitial iron concentration measured from the mediumly and highly contaminated wafers, respectively, and the single colored and hatched bars depict the measured interstitial iron concentration values before and after the dissolution anneals respectively. The emitter parameters used in this figure are justified in Section 5.3. No segregation was simulated here.*

5.3 Gettering properties of the implanted emitter

After the density of precipitation sites in the bulk and at the silicon-oxide interface was determined, the properties of the emitter were investigated. More specifically, the unknown parameters remaining were the density of precipitation sites at the implanted emitter and the segregation coefficient of the emitter. As reasoned in Section. 4.2, the dominant gettering mechanism was assumed to be precipitation and most of the precipitation sites were assumed to be at the first 100 nm of the wafer, most probably in the structural defects caused by implantation. Thus, at first the gettering anneals were simulated without any segregation effect at all. As can be seen from Fig. 10, the gettering effect of all the anneals are quite well explained by precipitation only, except that according to simulations, there is no precipitation-caused [Fe_i] drop at all for the mediumly contaminated 800 °C and 750 °C samples. After fixing the precipitation properties, the segregation coefficient was estimated based on the drop in [Fe_i] caused by the gettering anneals in the mediumly

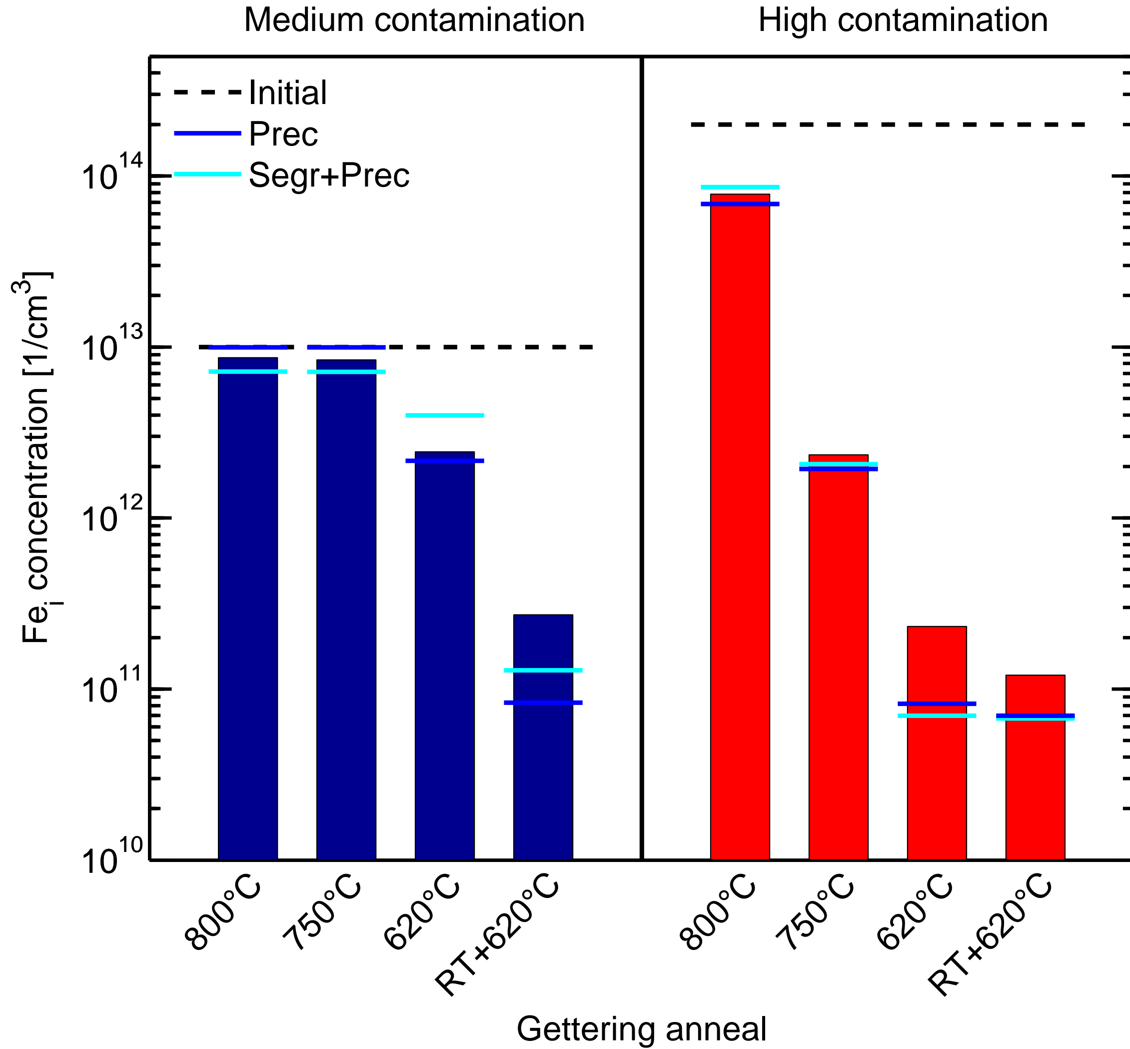

Figure 10: *Gettering efficiency of the gettering anneals illustrated in Fig. 7 as reported earlier [5] compared to simulation results. The blue and red bars depict mediumly and highly contaminated wafers.*

contaminated 800 °C and 750 °C samples. The phosphorus profile measured from the 620 °C sample after gettering by SIMS [5] was used in the simulations. The phosphorus profile was assumed to remain unchanged throughout the process. The simulation results including the segregation are also depicted in Fig. 10.

Table 4: *The simulated density of precipitation sites throughout the wafers.*

Wafer part	Density of precipitation sites [cm^{-3}]
Emitter	$8.3 \cdot 10^{12}$
Bulk	$3.3 \cdot 10^{5}$
Silicon-oxide interface	$2 \cdot 10^{10}$

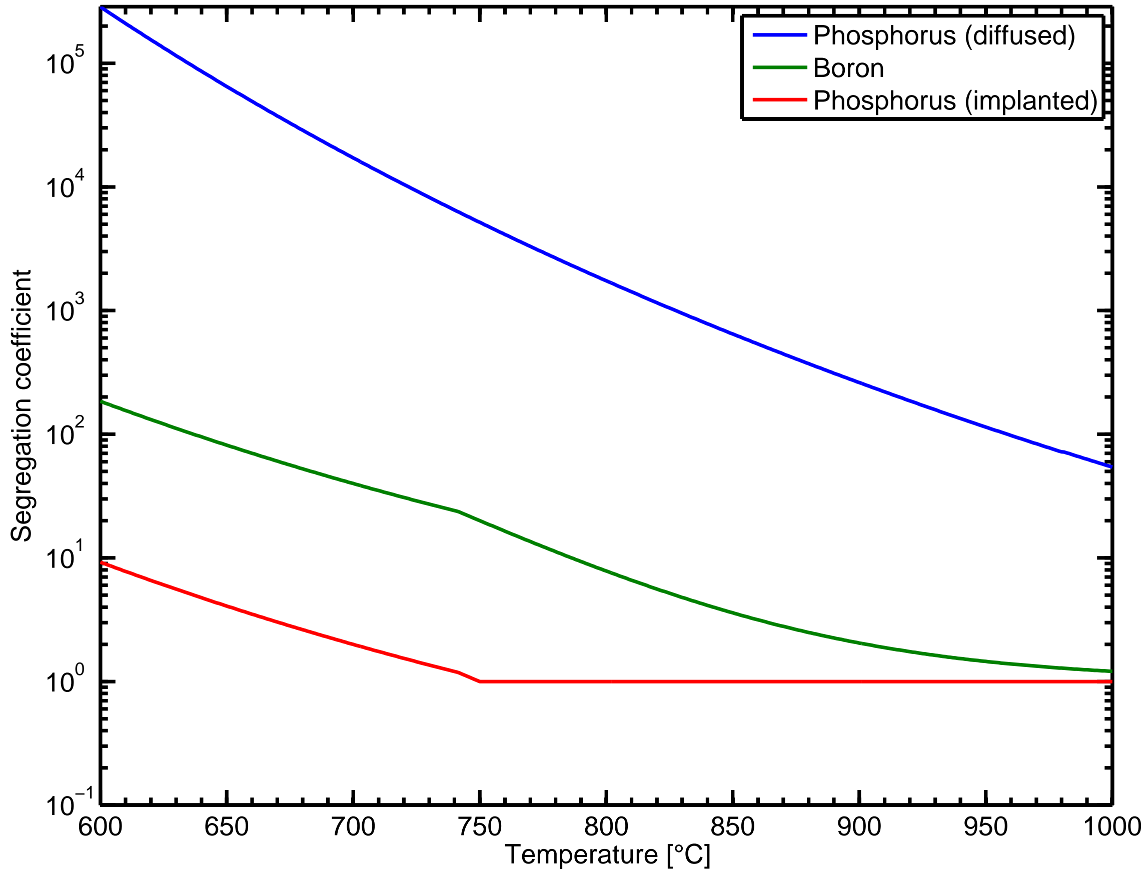

Figure 11: *The segregation coefficient used in this work compared to the segregation coefficient previously calculated for a similar concentration of boron and diffused phosphorus. The natural assumption that the segregation coefficient cannot be less than one was made in the simulations.*

The density of precipitation sites at the emitter, which produced optimal simulation results was $8 \cdot 10^{12}$ cm^{-3}. The precipitation site densities used throughout the wafer are tabulated in Tab. 4. The segregation coefficient used in Fig. 10 is 20 times smaller than that of the same concentration of boron, which is given by Eq. (29). This is interesting because in the traditional dopant in-diffusion, phosphorus has previously been noted to achieve a higher gettering efficiency than boron [8]. Additionally, the segregation coefficient for diffused phosphorus has previously been estimated to be considerably higher [32]. For comparison, the segregation coefficient used in this work and earlier calculated segregation coefficients for a similar boron and diffused phosphorus concentration are illustrated in Fig. 11. It can be seen that the predicted segregation coefficient for implanted phosphorus is larger than one only for temperatures below 750 °C. This means that the gettering efficiency simulated in the mediumly contaminated 800 °C and 750 °C samples was caused during exponential cool down after the gettering anneal, adding uncertainty to the calculated segregation coefficient.

Another interesting point is that according to the simulation results, the highly contaminated 620 °C and RT+620 °C samples should be gettered up to the solubility limit at

620 °C, which is approximately $9 \cdot 10^{10}$atoms/cm^3 according to Eq. (20), and then drop slightly below this during the pull out from the gettering furnace. This could be a sign of some factor hindering precipitation in these samples, one possibility being the effect of immobile iron in the presence of phosphorus as described in section 2.4. This hypothesis is supported also by the fact that 1) adding the effect of segregation does reduce the simulated gettering efficiency in the mediumly contaminated RT+620 °C sample and 2) the gettering efficiency in the highly contaminated RT+620 °C sample *without* an emitter was higher than in the RT+620 °C sample *with* emitter, as is shown in Fig. 9. However, if the effect of immobile iron is as predicted by Eq. (39), the segregation coefficient should be high enough to cause a stronger gettering effect in the mediumly contaminated 800 °C and 750 °C samples. It should be noted that the assumption of the constant phosphorus profile throughout the gettering anneal could possibly cause the simulations to underestimate the segregation coefficient, but large changes to the phosphorus profile are unlikely, as a very similar phosphorus profile was measured from the 800 °C sample as well.

5.3.1 Assessment of assumptions for SPV measurements

When calulating the interstitial iron concetrations depicted in Fig. 10 based on SPV measurements, several assumptions of the physical circumstances were made. Namely, in derivation of Eq. (69) it was assumed that the minority carrier diffusion length is much smaller than the sample width and in Eq. (72), it is implicitly assumed that the diffusion length is limited by FeB pairs before dissociating them and by interstitial iron after the dissociation. To assess the justification of these assumptions, the diffusion lenghts of selected samples are illustrated in Fig. 12. From Fig. 12a it can immediately be seen, that the diffusion lengths of many samples before dissociating the FeB pairs are not neglibile when compared to the wafer thickness of 400 µm. Especially, the diffusion length in the highly contaminated 620 °C sample is around 550 µm, almost 1.5 times the wafer thickness. Thus, especially the diffusion lenghts measured before dissociation from the highly contaminated 620 °C and the mediumly contaminated RT+620 °C samples should be treated with caution, because at higher diffusion lenghts, the recombination of charge carriers at the back surface of the wafers can have a noticable effect on the measured diffusion length value [46].

A reliable method to assess the validity of the assumption regarding the diffusion length limiting species is to observe the ratio of the diffusion lengths measured before and after dissociation of the FeB pairs. To facilitate this, the aforementioned ratios are calculated in Fig. 12b. It can be seen that in both the highly and mediumly contaminated 620 °C sample, the ratio of the measured diffusion lenghts is approximately 3. According to theory, this is the expected ratio in the case when the diffusion length is limited by FeB pairs before the dissociation and by interstitial iron after the dissociation [46], suggesting that the measured interstitial iron concentrations in both these samples are close to the actual value.

However in the RT+620 °C samples, the ratio is less than what is predicted by theory. In the lowly contaminated sample, the ratio is little over 2 and in the highly contaminated it is

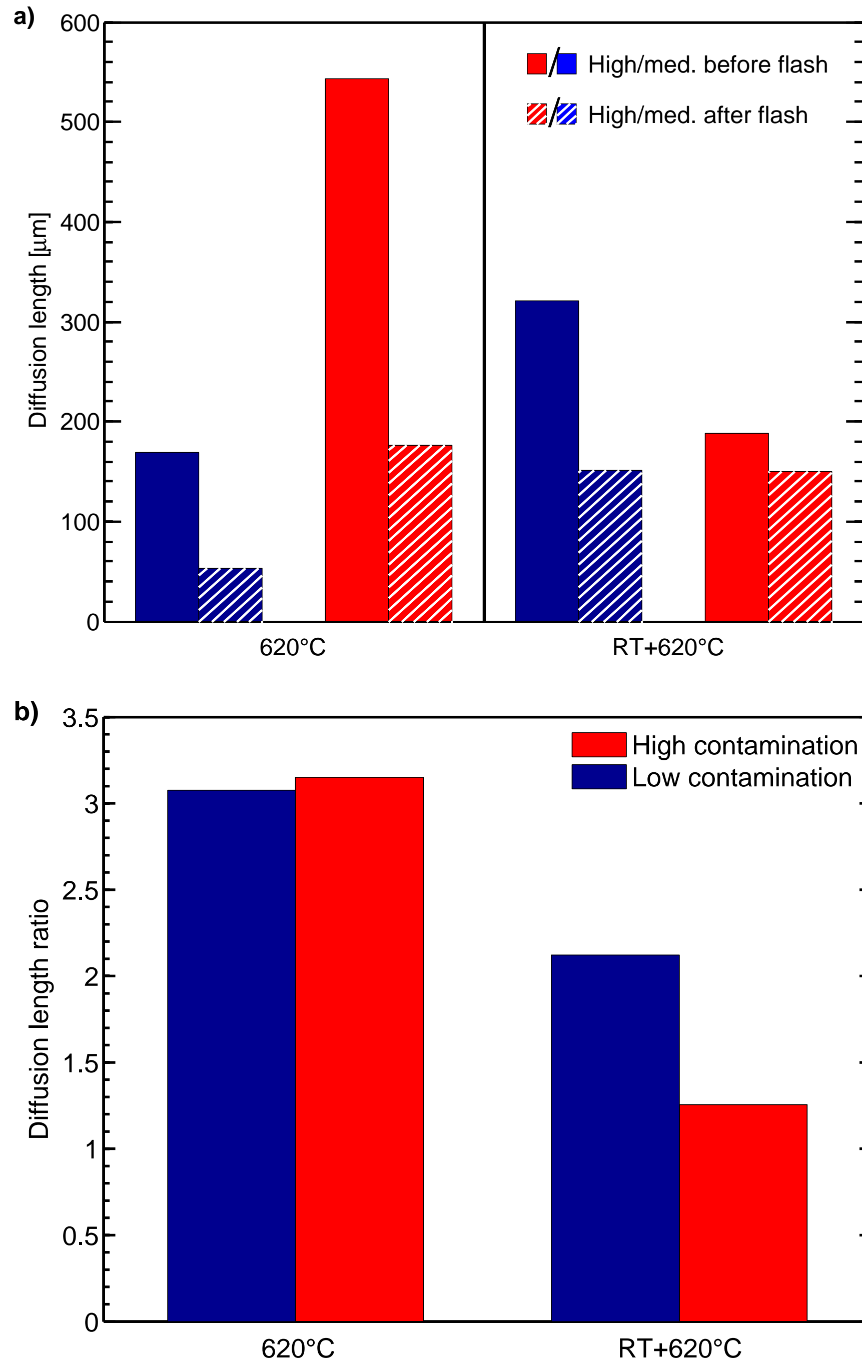

Figure 12: *a) The diffusion lengths of selected samples measured before and after dissociating the FeB pairs by flashlight and b) their ratio are highlighted. The diffusion lengths measured before the flash have been reported previously [5].*

less than 1.5. This suggests, that the diffusion length prior the dissociation of the FeB pairs is not limited by interstitial iron, which, subsequently, results in a measured interstitial iron concentration, which underestimates the actual iron concentration value. In section 5.1, it was hypothesized that the limiting species was bulk precipitates, but since the diffusion length before the dissociation of the FeB pairs is around half the wafer thickness, it is difficult to fully distinguish the effect of bulk precipitates from the recombination at the back surface.

5.4 Simulated precipitate size distributions after processing

5.4.1 Precipitates at the emitter

After fixing the simulation paramaters, the hypothesis of the different precipitate size distributions was investigated by simulating the precipitate size distribution after the gettering anneals at the emitters of the 750 °C, 620 °C and RT+620 °C samples with the iron simulator described in Section 2. The resulting precipitate size distributions are shown as a function of precipitate size in Fig. 13. Simulation results both with and without the segregation effect are shown. To make the results later comparable with the μ-XRF technique, the space dependent precipitate size distribution $f(n,x)$ was integrated over the μ-XRF information depth:

$$f_{\mathrm{XRF}}(n) = \int_{0}^{d_{\mathrm{inf}}} f(n,x)\mathrm{d}x, \tag{78}$$

where $f_{\mathrm{XRF}}(n)$ corresponds to the size distribution reachable by the μ-XRF technique. Thus, the function f_{XRF} actually describes the *areal* density of precipitates at and close to the emitter, precisely as μ-XRF. As an example, the areal density of precipitates located within d_{inf} of the wafer surface between sizes 10^4 and 10^5 atoms is given by $\int_{10^4}^{10^5} f_{\mathrm{XRF}}\mathrm{d}n$.

It should be noted that according to the simulations, the vast majority of the precipitates are contained within the first 100 nm under the emitter surface, where the implantation damage is assumed to be located. The simulated size distributions qualitatively support the hypothesis presented in Section 5.1. The 750 °C sample exhibits a low density of large precipitates, the peak of the distribution being around $2.5 \cdot 10^7$ atoms, which could be high enough to short the emitter. The low density of large precipitates is explained by the slow ramp to the relatively high gettering temperature of 750 °C, which inhibits widespread nucleation. In the 620 °C sample, on the other hand, the slow ramp continues up to 620 °C, which results in richer precipitation because the iron supersaturation increases going down from 750 °C to 620 °C. Also the gettering anneal in the 620 °C sample was longer (8 hours) than in the 750 °C sample (3.5 hours), which allowed the precipitates to grow, reaching almost as large sizes as in the 750 °C sample.

As opposed to the previous samples, the RT+620 °C sample experienced very strong nucleation during the room temperature pullout, where the supersaturation of iron is very

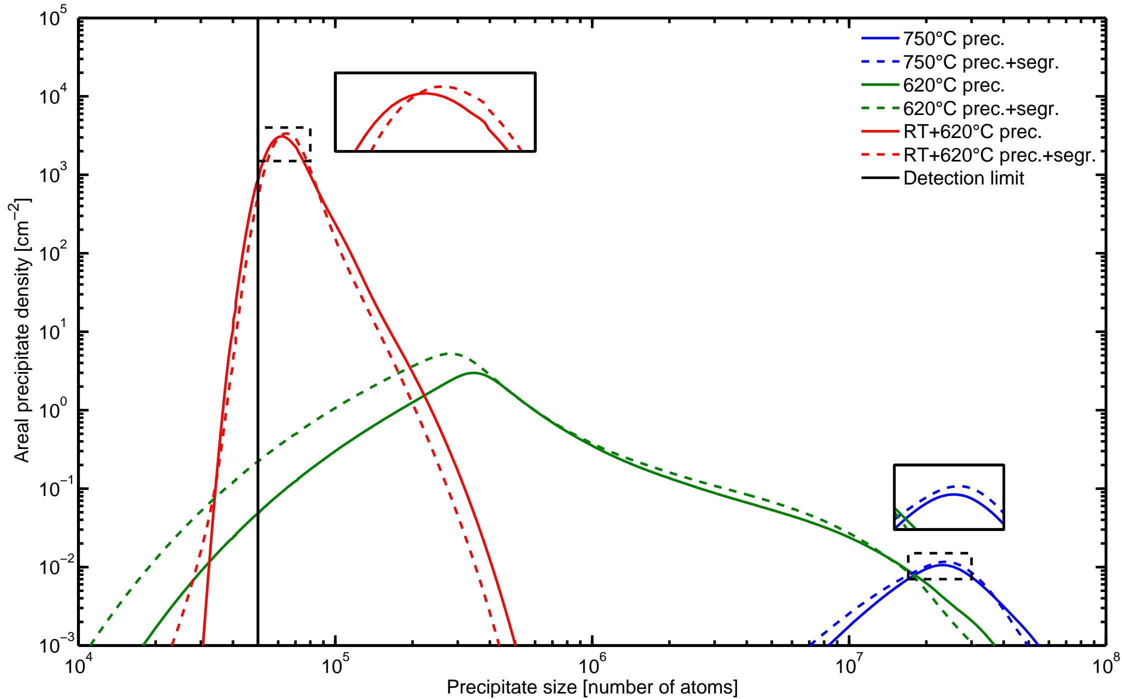

Figure 13: *Simulated precipitate size distributions on the emitter side within the information depth of the μ-XRF are shown for the highly contaminated 750 °C, 620 °C and RT+620 °C samples. The approximate detection limit of μ-XRF ($5 \cdot 10^4$ atoms) is shown as a black line.*

high but diffusivity low. The strong nucleation resulted in a high density of precipitates during the 8 h gettering anneal. Due to the high density in the RT+620 °C sample, the precipitates did not grow as large as in the C sample, because the total amount of iron is distributed among more precipitates. The average size of a precipitate in the RT+620 °C sample stays at around $6 \cdot 10^4$ atoms and a large share of the precipitates remain below the detection limit of the μ-XRF.

According to the simulated size distributions, the effect of segregation is not dominant, as is to be expected based on its relatively low impact on the gettering efficiency as stated in Section 5.3. It seems however, that adding the effect of segregation results in a slightly higher density of slightly smaller precipitates. This is probably because during the nucleation phase, the immobile phosphorus lowers the diffusivitity according to Eq. (39), which allows the precipitates to nucleate a longer time before the growth of existing precipitates begins to dominate as a precipitation mechanism.

5.4.2 Precipitates in the bulk

To study the hypothesis of the bulk precipitates causing the low diffusion length in the RT+620 °C sample, the total density of precipitates in the bulk after the gettering anneals was simulated for the 750 °C, 620 °C and the RT+620 °C samples. The results without simulating segregation are illustrated in Fig. 14. The results including the impact of segregation are omitted, because segregation had negligible impact on the results. It is shown that the RT+620 °C sample is predicted to have about twice the density of precipitates of the 620 °C sample and about 100 times the density of precipitates of the 750 °C sample.

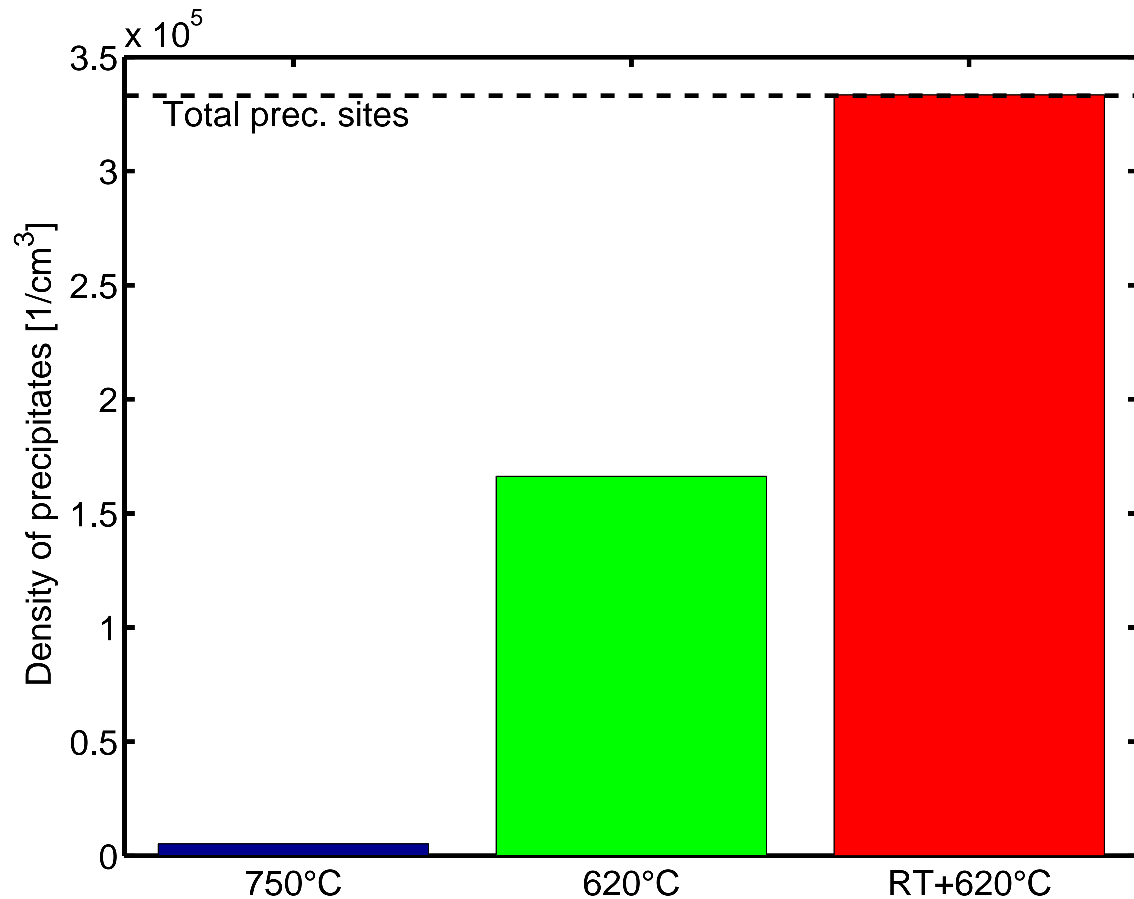

Figure 14: *The simulated density of precipitates after the gettering anneals for the 750 °C, 620 °C and the RT+620 °C sample are shown. The total density of precipitation sites in the bulk is indicated by the dashed line. The segregation effect was not simulated for the values shown here.*

However, it should be noted that in the RT+620 °C sample, all the precipitation sites are occupied, meaning that by using these parameters, it would be impossible to simulate a higher density of precipitates. Based on the simulated size distributions at the emitter, it would be reasonable that the discrepancy in the bulk precipitate densities between the RT+620 ° and 620 ° samples would be of the same order as that between the 750 °C and

620 °C samples. Thus, it is likely that the bulk density of precipitates in the RT+620 °C sample is underestimated here and the density of bulk precipitates in the RT+620 °C sample could well be high enough to cause the low minority carrier lifetime in the bulk as discussed in Section 4.2.

The underlying cause for the underestimation of the bulk precipitate density in the RT+620 °C is most likely in the procedure, how the density of precipitation sites was assessed. The indirect method of calculating the density through the amount of iron precipitated in the bulk during processing, as described in Section 5.2, might not accurately estimate the density of precipitation sites. It could be that the precipitation sites differ not only quantitatively, but also qualitatively from the precipitation sites at the emitter, meaning that the nucleation at the precipitation sites in the bulk is less accessible as in the precipitation sites at the emitter. This could be simulated by for example setting a smaller capture radius for the precipitation sites in the bulk. The difficulty of this discussion is the estimation as to where excatly does iron precipitate in the bulk: Is it oxygen precipitates, structural dislocations or something else? Lastly, it could also be that nucleation during the room temperature pullout is too rapid that the nucleation paramaters fitted in Section 2.7 no longer accurately describe the process.

6 Verification of simulation results by the μ-XRF method

To validate the simulated precipitation site densities presented in section 5.4.1, the highly contaminated 750 °C, 620 °C and RT+620 °C samples were investigated by μ-XRF. An area of several hundreds of μm^2 was measured from each sample and the resulting fluorescent counts were converetd into iron loadings in $\mu g/cm^2$. The raw data maps are shown in Fig. 15. Precipitates are detected in each sample, but their sizes and density vary. In this section, the precipitates are distinguished from the noise and the sizes of the precipitates are quantified and compared to the simulation results presented in Section 5.4.1.

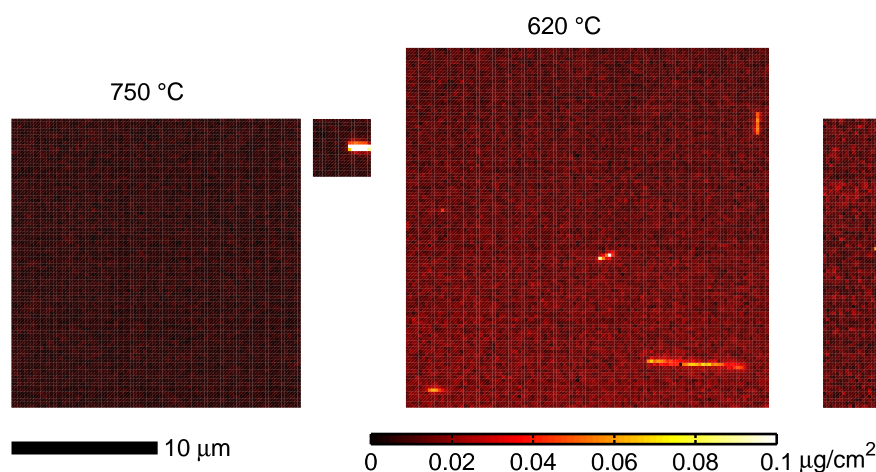

Figure 15: *Measured* μ-XRF *data maps and iron load from highly contaminated 750 °C, 620 °C and RT+620 °C samples are shown. The scale bar is 10 μm. The bright spots in the maps correspond to iron precipitates. The two maps on the left are both from the B sample. Pixel size is 220 nm in each sample.*

6.1 Distinguishing precipitates from noise

The real precipitates are distinguished from the noise by fitting all the pixel readings in each data map on a truncated normal distribution as described in Section 3.2.3. Histograms from all the pixel values are illustrated for each measured data map in Fig. 16. The resulting statistical noise limits calculated from the truncated normal distribution are also shown.

To ensure that defining the statistical noise limit this way does not result in noise pixels being mistaken as real pixels, the statistical noise limits are compared to the minimum detection limit of the 2-ID-D beamline for each measurement. The minimum detection limit is a theoretical construct calculated from the signal-to-noise ratio of the beamline. The statistical noise limits and the minimum detection limits are compared in Tab. 5. For the C and D maps and the small B map, the minimum detection limit is lower than the statistical noise limit and thus everything above the statistical noise limit can be regarded as real precipitates. However, for the large B map, the minimum detection limit is actually

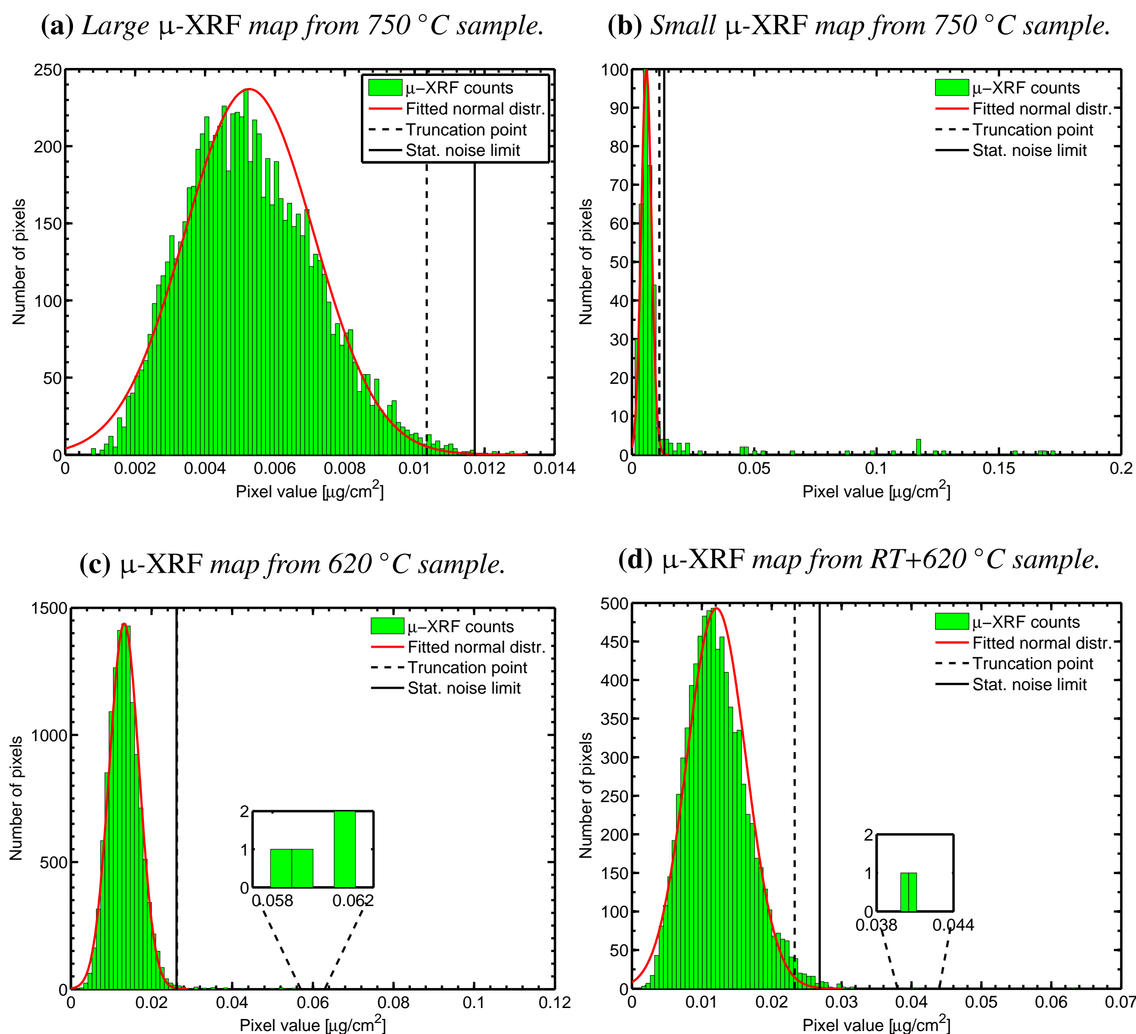

Figure 16: *THe histograms and statistical noise limits for the different* µ-XRF *data maps are shown. Also the truncation point for the truncated normal distribution is shown. The insets in figures c) and d) show examples of pixels with a high Fe loading.*

higher than the statistical noise limit. In fact, it can be seen from Fig. 16a that no pixel value is above the minimum detection limit of 0.015 μg/cm^2 suggesting that the large B map does not contain a single precipitate.

It can also be seen from Tab. 5 that the statistical noise limit defined for the 620 °C sample is almost twice larger than the minimum detection limit. This means that instead of the $\mu + 3.5\sigma$ definition of the statistical noise limit, a slightly lower value could perhaps be used. This could reveal some more precipitates, whose sizes now fall beyond the statistical noise limit but which are still above the minimum detection limit. Previously, a definition of $\mu + 3\sigma$ has also been used as the statistical noise limit for similar μ-XRF data maps [61].

Table 5: *The statistical noise limits and minimum detection limits of each sample are compared.*

Map	Statistical noise limit [10^{-3} μg/cm^2]	Minimum detection limit [10^{-3} μg/cm^2]
Large map from 750 °C sample	11.7	15
Small map from 750 °C sample	13.3	15
620 °C sample	26.2	12.1
RT+620 °C sample	26.9	21

The data maps which contained precipitates are shown in Fig. 17 with noise filtered. It can be immediately seen from the maps that even though the samples are monocrystalline, precipitation of iron seems to be highly heterogeneous. Furthermore, the data maps suggest a process dependent precipitate size distribution. In the 416 μm^2 area studied from the 750 °C sample, only a single, large precipitate or precipitate cluster with a high Fe loading is found. On the contrary, in the 400 μm^2 area studied from the RT+620 °C sample, a total of 33 precipitates are detected, most of which fit within a single 220 nm pixel. The 620 °C sample shows also peculiar precipitate growth with the smallest precipitates contained within a single pixel and the largest precipitate or agglomerate spanning almost 7 μm in length with an aspect ratio approaching 15:1.

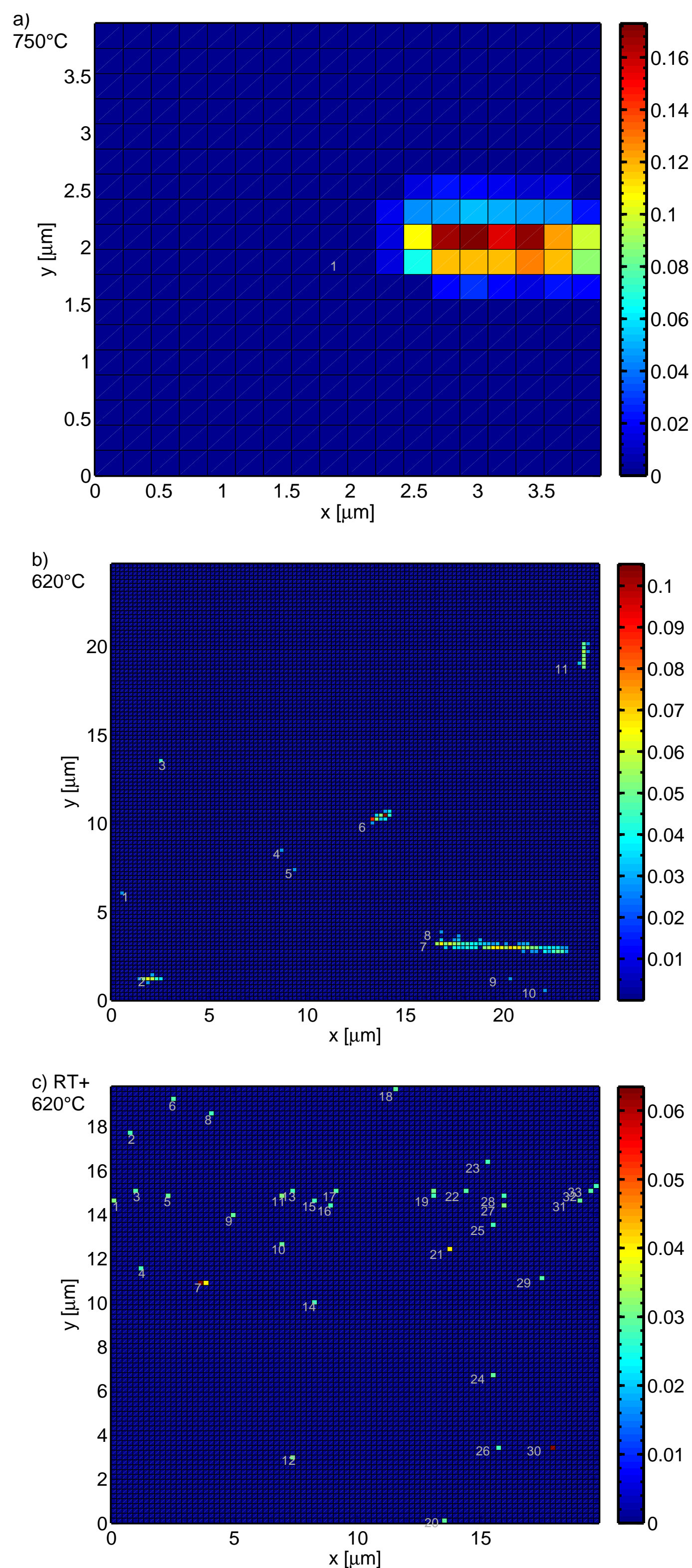

Figure 17: *The* µ-XRF *data maps are shown for a) the small map from the 750 °C sample, b) the 620 °C sample and c) the RT+620 °C sample with the noise filtered. A pixel with a reading of zero corresponds to noise. The colorbar shows the pixel Fe loadings in µg/cm^2. The detected precipitates are numbered and the pixel size is 220 nm.*

6.2 Comparing simulated and measured precipitate size distributions at the emitter

To quantitatively compare the simulated precipitate size distributions to the measured ones, the number of atoms per precipitate was calculated for the measured maps as described in Section 3.2.3. Then the areal precipitate densities predicted by the measured maps were counted for selected size intervals. For example, it was counted how many precipitates there were in the RT+620 °C map between sizes $9 \cdot 10^4$ atoms and $2.7 \cdot 10^5$ atoms and assuming that the precipitates are spread similarly throughout the whole wafer surface, an areal density estimate for the given size interval in the given sample was achieved. Similarly, the simulated size distribution f_{XRF} was integrated over these same intervals to reach a comparable density. The results are illustrated in Fig. 18.

The measured and simulated results correlate to a certain extent. In the 750 °C sample, the simulations predict that at the 416 μm^2 measured, one (or almost one) precipitate should be found, as was experimentally verified. The simulations predict that the found precipitate would contain slightly more iron than the measured precipipitate ($2.5 \cdot 10^7$ atoms instead of $8 \cdot 10^6$), but because only one precipitate was measured, a small discrepancy is understandable.

In the 620 °C sample, both simulations and measurements indicate the existence of both large and small precipitates, but the measured distribution is slightly uneven. A relatively high areal density ($1 \cdot 10^{-2} \mu m^{-2}$) of precipitates with sizes between $8.6 \cdot 10^4$ and $2.6 \cdot 10^5$ atoms was measured while no precipitates with sizes between $2.6 \cdot 10^5$ and $7.8 \cdot 10^5$ atoms were found. Similar behavior is observed for the next two size bins of Fig. 18b as well. This could possibly be explained by the fact that the density of the precipitates in the empty bins is so close to the limit density, that these precipitates were simply not observed in the 625 μm^2 map measured from the 620 °C sample.

Other possible explanations are that the inclusion of all pixels above noise when counting the precipitate sizes overestimates the precipitate sizes or that there are actually multiple precipitates counted within single precipitates. If for example the single precipitate measured in the bin between $7 \cdot 10^6$ and $2.1 \cdot 10^7$ atoms would include 2-3 precipitates between $2.6 \cdot 10^5$ and $7.8 \cdot 10^5$ atoms, the measured distribution would be more in congruence with the simulated distribution. However, this would also suggest that the actual precipitate size distribution falls off more rapidly with higher atom sizes as the simulated distributions would predict. In any case, it is highly likely that there are in fact quite large precipitates in the 620 °C sample containing at least over 10^6 atoms, which is most likely enough to short the emitter as hypothesized in Section 5.1.

In the RT+620 °C sample, both simulations and measurements predict a high density of small precipitates with sizes very close to the detection limit. Simulations predict that there is a notable amount of precipitates also with sizes right below the detection limit. This is also supported by the histogram from the μ-XRF map of the RT+620 °C sample in Fig. 16d, where there are slightly more measured histogram counts right below the detection limit than the Gaussian fit for the noise would suggest. It is likely that these counts contain a considerable amount of real precipitates.

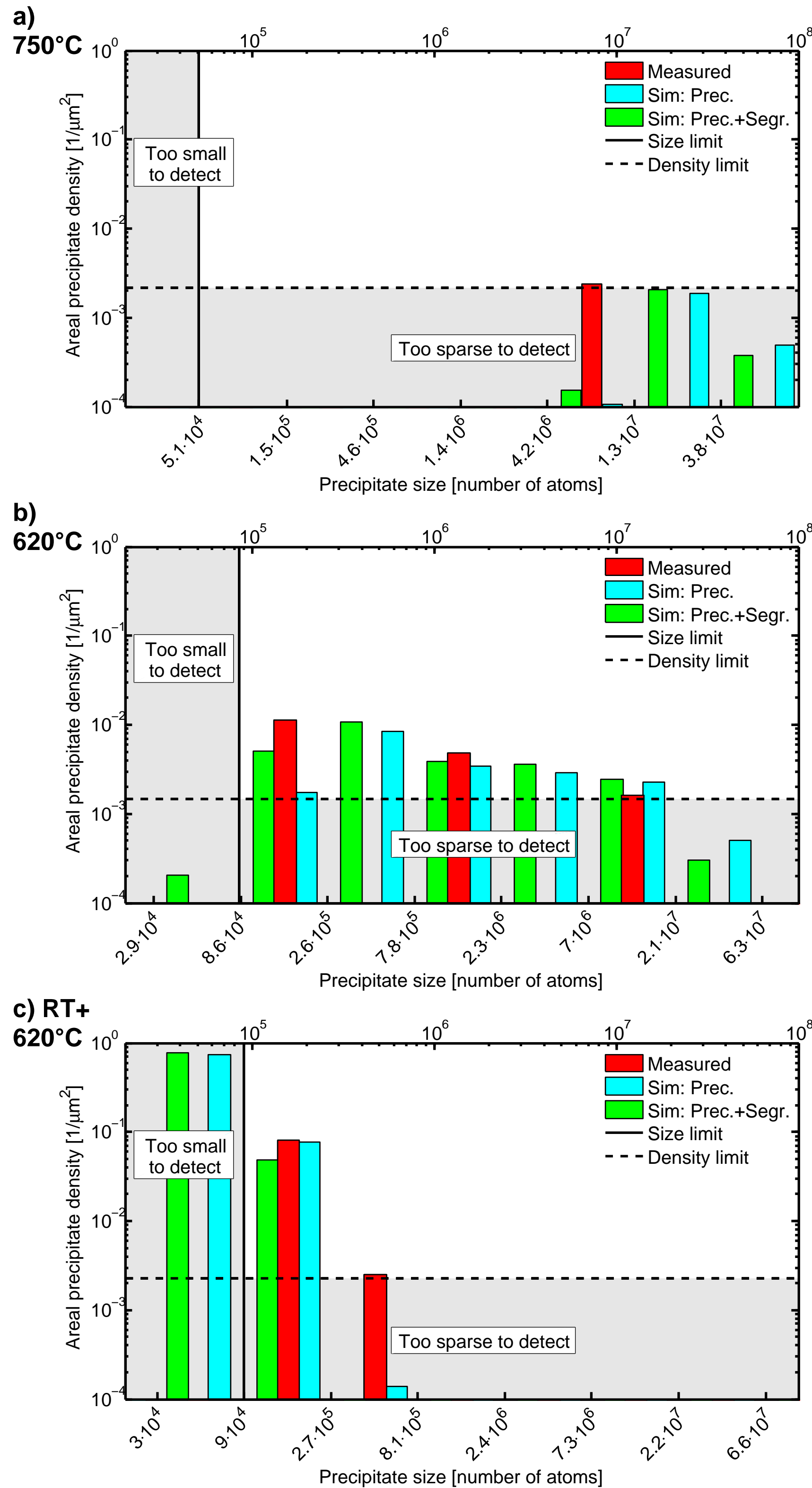

Figure 18: *Comparison of the simulated and measured iron precipitate size distributions at the emitter of a) the 750 °C b) the 620 °C and c) the RT+620 °C samples. The measurement results both with and without the effect of segregation are shown. Also the minimum detectable size and the minimum detectable density are shown.*

7 Conclusions

The main experimental finding of this work is that when gettering iron in silicon solar cells with phosphorus-implanted emitters, not only the reduction of interstitial iron but also the iron precipitate size distribution can have an effect on macroscopic cell properties. Precipitate size distributions after different gettering anneals were quantified with the theoretical model presented in this work and verified by μ-XRF measurements. It was shown that slow cooling from activation annealing temperatures to a moderate gettering temperature can produce large precipitates at the emitter, in some cases >1 μm in size which can short circuit the emitter. Large precipitates can be avoided and simultaneously an adequately low interstitial iron concentration can be reached by quenching the samples before the gettering anneal. However, this seems to result in widespread precipitation throughout the sample, possibly leading up to a low minority charge carrier diffusion length in the bulk.

In this work, the modeled size distributions correlated with the measured distributions in the emitter, suggesting that the behavior of the precipitate size distribution can be predicted to some extent if the kinetics of the precipitation process are first estimated based on the gettering efficiency of the anneals. Thus, if the precipitation kinetics, mainly the number of precipitation sites and their capture radius, can be estimated based on the implantation and gettering parameters, also the size distribution can most likely be estimated correctly. However, it is difficult to predict how many precipitation sites are exactly induced by implantation damage, partly because also the recovering effect of the implantation anneal has to be taken into account. Another vital step needed in the future is the quantitative estimation of the morphology and dimensions of the precipitates at the emitter to be able to assess if they have the potential to short the emitter solely based on the theoretical size distribution. Similarly, the link between the bulk precipitate size distribution and the bulk minority carrier diffusion length requires further work.

References

[1] V. Prajapati, T. Janssens, J. John, J. Poortmans and R. Mertens, Diffusion-free high efficiency silicon solar cells, *Progress in Photovoltaics: Research and Applications*, **21**(5), pp. 980–985 (2013).

[2] A. Rohatgi, D. L. Meier, B. McPherson, Y.-W. Ok, A. D. Upadhyaya, J.-H. Lai and F. Zimbardi, High-throughput ion-implantation for low-cost high-efficiency silicon solar cells, *Energy Procedia*, **15**, pp. 10–19 (2012).

[3] S. Myers, M. Seibt and W. Schröter, Mechanisms of transition-metal gettering in silicon, *Journal of Applied Physics*, **88**(7), pp. 3795–3819 (2000).

[4] R. Hopkins and A. Rohatgi, Impurity effects in silicon for high efficiency solar cells, *Journal of Crystal Growth*, **75**(1), pp. 67–79 (1986).

[5] V. Vähänissi, A. Haarahiltunen, M. Yli-Koski and H. Savin, Gettering of iron in silicon solar cells with implanted emitters, *IEEE Journal of Photovoltaics*, **4**(1), pp. 142–147 (2014).

[6] M. Aoki, A. Hara and A. Ohsawa, Fundamental properties of intrinsic gettering of iron in a silicon wafer, *Journal of Applied Physics*, **72**(3), pp. 895–898 (1992).

[7] J. D. Muprhy and R. Falster, Contamination of silicon by iron at temperatures below 800 °C, *physica status solidi (RRL) - Rapid Research Letters*, **5**(10-11), pp. 370–372 (1999).

[8] H. Talvitie, V. Vähänissi, A. Haarahiltunen, M. Yli-Koski and H. Savin, Phosphorus and boron diffusion gettering of iron in monocrystalline silicon, *Journal of Applied Physics*, **109**(9) (2011).

[9] A. Haarahiltunen, H. Väinölä, O. Anttila, M. Yli-Koski and J. Sinkkonen, Experimental and theoretical study of heterogeneous iron precipitation in silicon, *Journal of Applied Physics*, **101**(4), p. 043507 (2007).

[10] J. Hofstetter, D. Fenning, M. Bertoni, J. F. Lelièvre, C. del Cañizo and T. Buonassisi, Impurity-to-efficiency simulator: predictive simulation of silicon solar cell performance based on iron content and distribution, *Progress in photovoltaics: Research and applications*, **19**, pp. 487–497 (2011).

[11] A. Istratov, H. Hieslmair and E. Weber, Iron and its complexes in silicon, *Applied Physics A*, **69**, pp. 13–44 (1999).

[12] A. Istratov, H. Hieslmair and E. Weber, Iron contamination in silicon technology, *Applied Physics A*, **70**(5), pp. 489–534 (2000).

[13] G. Coletti, R. Kvande, V. D. Mihailetchi, L. J. Geerligs, L. Arnberg and E. J. Øvrelid, Effect of iron in silicon feedstock on p- and n-type multicrystalline silicon solar cells, *Journal of Applied Physics*, **104**(10), 104913 (2008).

[14] T. Buonassisi, A. A. Istratov, M. D. Pickett, M. Heuer, J. P. Kalejs, G. Hahn, M. A. Marcus, B. Lai, Z. Cai, S. M. Heald, T. F. Ciszek, R. F. Clark, D. W. Cunningham, A. M. Gabor, R. Jonczyk, S. Narayanan, E. Sauar and E. R. Weber, Chemical natures and distributions of metal impurities in multicrystalline silicon materials, *Progress in Photovoltaics: Research and Applications*, **14**(6), pp. 513–531 (2006).

[15] E. Olsen and E. J. Øvrelid, Silicon nitride coating and crucible — effects of using upgraded materials in the casting of multicrystalline silicon ingots, *Progress in Photovoltaics: Research and Applications*, **16**(2), pp. 93–100 (2008).

[16] T. Buonassisi, A. A. Istratov, M. Heuer, M. A. Marcus, R. Jonczyk, J. Isenberg, B. Lai, Z. Cai, S. Heald, W. Warta, R. Schindler, G. Willeke and E. R. Weber, Synchrotron-based investigations of the nature and impact of iron contamination in multicrystalline silicon solar cells, *Journal of Applied Physics*, **97**(7), 074901 (2005).

[17] V. Vähänissi, A. Haarahiltunen, H. Talvitie, M. Yli-Koski and H. Savin, Impact of phosphorus gettering parameters and initial iron level on silicon solar cell properties, *Progress in Photovoltaics: Research and Applications*, **21**(5), pp. 1127–1135 (2013).

[18] D. P. Fenning, J. Hofstetter, A. E. Morishige, D. M. Powell, A. Zuschlag, G. Hahn and T. Buonassisi, Darwin at high temperature: Advancing solar cell material design using defect kinetics simulations and evolutionary optimization, *Advanced Energy Materials* (2014).

[19] V. Alex, S. Finkbeiner and J. Weber, Temperature dependence of the indirect energy gap in crystalline silicon, *Journal of Applied Physics*, **79**(9), pp. 6943–6946 (1996).

[20] H. Ibach and H. Lüth, *Solid-State Physics*, Springer-Verlag, Berlin, Germany, 2nd ed. (2006).

[21] A. A. Istratov, W. Huber and E. R. Weber, Modeling of competitive gettering of iron in silicon integrated circuit technology, *Journal of the Electrochemical Society*, **150**(4), pp. G244–G252 (2003).

[22] H. P. D. Lanyon and R. A. Tuft, Bandgap narrowing in moderately to heavily doped silicon, *IEEE Transactions on Electron Devices*, **26**(7), pp. 1014–1018 (1979).

[23] W. B. Joyce and R. W. Dixon, Analytic approximations for the Fermi energy of an ideal Fermi gas, *Applied Physics Letters*, **31**(5), pp. 354–356 (1977).

[24] K. F. Brennan, *The Physics of Semiconductors with applications to optoelectronic devices*, Cambridge University Press, Cambridge, United Kingdom (1999).

[25] H. Lemke, Energieniveaus und Bindungsenergien von Ionenpaaren in Silizium, *physica status solidi (a)*, **76**, pp. 223–234 (1983).

[26] L. C. Kimerling and J. L. Benton, Electronically controlled reactions of interstitial iron in silicon, *Physica*, **116B**, pp. 297–300 (1983).

[27] H. Reiss, C. Fuller and F. J. Morin, Chemical interactions among defects in germanium and silicon, *The Bell System Technical Journal*, **35**(3), pp. 535–636 (1956).

[28] A. A. Istratov, C. Flink, H. Hieslmair and E. E. Weber, Instrinsic diffusion coefficient of interstitial copper in silicon, *Physical Review Letters*, **81**(6), pp. 1243–1246 (1998).

[29] H. Kohno, H. Hieslmair, A. A. Istratov and E. R. Weber, Temperature dependence of the iron donor level in silicon at device processing temperatures, *Applied Physics Letters*, **76**(19), pp. 2734–2736 (2000).

[30] H. Hieslmair, A. A. Istratov, C. Flink, S. A. McHugo and E. R. Weber, Experiments and computer simulations of iron profiles in p/p+ silicon: segregation and the position of the iron donor level, *Physica B*, **273-274**, pp. 441–444 (1999).

[31] M. Sanati, N. Gonzalez and S. K. Estreicher, Interstitial Fe in Si and its interactions with hydrogen and shallow dopants, *Physical Review B*, **76**, p. 125204 (2007).

[32] A. Haarahiltunen, H. Savin, M. Yli-Koski, H. Talvitie and J. Sinkkonen, Modeling phosphorus diffusion gettering of iron in single crystal silicon, *Journal of Applied Physics*, **99**, p. 064502 (2006).

[33] D. Gilles, W. Schröter and W. Bergholz, Impact of the electronic structure on the solubility and diffusion of 3*d* transition elements in silicon, *Physical Review B*, **41**(9), pp. 5770–5782 (1990).

[34] R. Kaischew and I. N. Stranski, On the kinetic deflection rate of germ formation, *Zeitschrift für Physikalische Chemie*, **B 26**, pp. 317–326 (1934).

[35] N. N. Tunitskii, On the condensation of supersaturated vapors, *Zhurnal Fizicheskoi Khimii*, **15**, pp. 1061–1071 (1941).

[36] D. Kaschiev, *Nucleation: basic theory with applications*, Butterworth-Heinemann, Massachusetts, United States (2000).

[37] H. Hieslmair, A. A. Istratov, S. A. McHugo, C. Flink, T. Heiser and E. R. Weber, Gettering of iron by oxygen precipitates, *Applied Physics Letters*, **72**, pp. 1460–1462 (1998).

[38] F. S. Ham, Theory of diffusion-limited precipitation, *Journal of Physics and Chemistry of Solids*, **6**(4), pp. 335–351 (1958).

[39] D. Gilles, E. R. Weber and S. Hahn, Mechanism of internal gettering of interstitial impurities in Czochralski-grown silicon, *Phys. Rev. Lett.*, **64**, pp. 196–199 (1990).

[40] S. T. Dunham, Growth kinetics of disk-shaped extended defects with constant thickness, *Applied Physics Letters*, **63**, pp. 464–466 (1993).

[41] A. Haarahiltunen, H. Talvitie, H. Savin, O. Anttila, M. Yli-Koski, M. I. Ashgar and J. Sinkkonen, Gettering of iron in silicon by boron implantation, *Journal of Material Science: Materials in Electronics*, **19**, pp. S41–S45 (2008).

[42] T. Tan, R. Gafiteanu, S. Joshi and U. Gösele, Science and modeling of impurity gettering in silicon, *Semiconductor Silicon 1998*, **98**, p. 1051 (1998).

[43] H. Hieslmair, S. Balasubramanian, A. A. Istratov and E. R. Weber, Gettering simulator: physical basis and algorithm, *Semiconductor Science and Technology*, **16**, pp. 567–574 (2001).

[44] J. Chang and G. Cooper, A practical difference scheme for Fokker-Planck equations, *Journal of Computational Physics*, **6**(1), pp. 1–16 (1970).

[45] J. Schön, H. Habenicht, M. C. Schubert and W. Warta, Understanding the distribution of iron in multicrystalline silicon after emitter formation: Theoretical model and experiments, *Journal of Applied Physics*, **109**(6) (2011).

[46] O. J. Anttila and S. K. Hahn, Study on surface photovoltage measurement of long diffusion length silicon: Simulation results, *Journal of Applied Physics*, **74**(1), pp. 558–569 (1993).

[47] D. K. Schroder, *Semiconductor Material and Device Characterization*, John Wiley & Sons, Inc., Hoboken, New Jersey, United States, 3rd ed. (2006).

[48] G. Zoth and W. Bergholz, A fast, preparation-free method to detect iron in silicon, *Journal of Applied Physics*, **67**(11), pp. 6764–6771 (1990).

[49] M. Yli-Koski, M. Palokangas, V. Sokolov, J. Storgårds, H. Väinölä, H. Holmberg and J. Sinkkonen, Recombination activity of iron in boron doped silicon, *Physica Scripta*, **T101**, pp. 86–88 (2002).

[50] A. Haarahiltunen, H. Väinölä, M. Yli-Koski, E. Saarnilehto and J. Sinkkonen, Detection of iron contamination in internally gettered p-type silicon wafers by lifetime measurements, in C. L. Claeys, M. Watanabe, R. Falster and P. Stallhofer, editors, *The Electrochemical Society Proceedings*, vol. 05 of *High Purity Silicon VIII*, pp. 160–164 (2004).

[51] D. P. Fenning, J. Hofstetter, M. I. Bertoni, G. Coletti, B. Lai, C. del Cañizo and T. Buonassisi, Precipitated iron: A limit on gettering efficacy in multicrystalline silicon, *Journal of Applied Physics*, **113**(4) (2013).

[52] J. Schön, A. Haarahiltunen, H. Savin, D. Fenning, T. Buonassisi, W. Warta and M. Schubert, Analyses of the evolution of iron-silicide precipitates in multicrystalline silicon during solar cell processing, *IEEE Journal of Photovoltaics*, **3**(1), pp. 131–137 (2013).

[53] T. S. Fell, P. R. Wilshaw and M. D. De Coteau, EBIC investigations of dislocations and their interactions with impurities in silicon, *physica status solidi (a)*, **138**(2), pp. 695–704 (1993).

[54] Z. Cai, B. Lai, W. Yun, I. McNulty, A. Khounsary, J. Maser, P. Ilinski, D. Legnini, E. Trakhtenberg, S. Xu, B. Tieman, G. Wiemerslage and E. Gluskin, Performance of a high-resolution x-ray microprobe at the Advanced Photon Source, *AIP Conference Proceedings*, **521**(1), p. 31 (2000).

[55] S. Kraft, J. Stämpel, P. Becker and U. Kuetgens, High resolution x-ray absorption spectroscopy with absolute energy calibration for the determination of absorption edge energies, *Review of Scientific Instruments*, **67**(3), pp. 681–687 (1996).

[56] G. Hölzer, M. Fritsch, M. Deutsch, J. Härtwig and E. Förster, $K\alpha_{1,2}$ and $K\beta_{1,3}$ x-ray emission lines of the $3d$ transition metals, *Physical Review A*, **56**, pp. 4554–4568 (1997).

[57] J. Hubbell and S. Seltzer, Tables of x-ray mass attenuation coefficients and mass energy-absorption coefficients (version 1.4), Available: http://www.nist.gov/pml/data/xraycoef/index.cfm, Accessed: 24th July, 2014.

[58] S. Vogt, MAPS : A set of software tools for analysis and visualization of 3d x-ray fluorescence data sets, *J. Phys. IV France*, **104**, pp. 635–638 (2003).

[59] P. S. Plekhanov and T. Y. Tan, Schottky effect model of electrical activity of metallic precipitates in silicon, *Applied Physics Letters*, **76**(25), pp. 3777–3779 (2000).

[60] J. Hofstetter, D. P. Fenning, J.-F. Lelièvre, C. del Cañizo and T. Buonassisi, Engineering metal precipitate size distributions to enhance gettering in multicrystalline silicon, *physica status solidi (a)*, **209**(10), pp. 1861–1865 (2012).

[61] D. Fenning, A. Zuschlag, M. Bertoni, B. Lai, G. Hahn and T. Buonassisi, Improved iron gettering of contaminated multicrystalline silicon by high-temperature phosphorus diffusion, *Journal of Applied Physics*, **113**(21) (2013).

A Ratio of neutral and ionized interstitial iron in silicon

Interstitial iron in silicon can be present in either neutral form or in ionized form depending whether the donor level formed by the interstitial atom is occupied by a hole or an electron. The ratio of the concentration of these two species is derived in this appendix with the help of Fermi-Dirac statistics and probability theory. The ratio of the concentration of neutral interstitial iron to the total concentration of interstitial iron corresponds to the occupation probability of the iron donor level. In the non-degenerate case, this is given by the Fermi-Dirac distribution evaluated at the iron donor level:

$$f_{\mathrm{FD}}(E_{\mathrm{D}}, T) = \frac{1}{\exp\left[\left(E_{\mathrm{D}} - E_{\mathrm{F}}\right)/k_{\mathrm{B}}T\right] + 1}. \tag{A1}$$

However, Eq. (A1) does not account for the fact that the donor level can be occupied by either a spin up or spin down electron. Accounting for spin-degeneracy and the fact that the donor state created by a single iron atom can be occupied by only one spin up or one spin down electron, the occupation probability of a single donor state is then given by the conditional probability:

$$P(occupied) = P\left(\uparrow \vee \downarrow \mid \neg 2A\right) = \frac{P(\uparrow \veebar \downarrow)}{P(\neg 2A)}, \tag{A2}$$

where $\vee$ is the logical OR operator, $\veebar$ the exclusive OR operator, the symbols "$\uparrow$" and "$\downarrow$" refer to the events "the state is occupied by a spin up electron" and "the state is occupied by a spin down electron", respectively and "2A" refers to the event "the state is occupied by two atoms". Now the spin up and spin down states can be thought as two separate states, whose independent occupation probabilities are given by Eq. (A1), leading up to the expression:

$$P(occupied) = \frac{P\left((\uparrow \wedge \neg \downarrow) \vee (\neg \uparrow \wedge \downarrow)\right)}{1 - P(2A)} \tag{A3}$$

$$= \frac{\frac{1}{1+B}\left(1 - \frac{1}{1+B}\right) + \left(1 - \frac{1}{1+B}\right)\frac{1}{1+B}}{1 - \left(\frac{1}{1+B}\right)^2}, \tag{A4}$$

where the assignment $\exp\left[\left(E_{\mathrm{D}} - E_{\mathrm{F}}\right)/k_{\mathrm{B}}T\right] \equiv B$ has been made to facilitate reading. Further algebra yields from Eq. (A4):

$$P(occupied) = \frac{\dfrac{2B}{(1+B)^2}}{\dfrac{B^2+2B}{(1+B)^2}} = \frac{2B}{B^2+2B} = \frac{1}{\frac{1}{2}B+1} \equiv \frac{1}{\frac{1}{2}\exp\left[(E_{\mathrm{D}}-E_{\mathrm{F}})/k_{\mathrm{B}}T\right]+1}. \quad \text{(A5)}$$

The ratio of the concentration of neutral interstitial iron to the total concentration of interstitial iron corresponds to the occupation probability of the iron donor level. In addition, the total concentration of interstitial iron is the sum of neutral interstitial iron and positively charged interstitial iron. Thus, the ratio of the concentrations of the charged and neutral interstial iron can be derived from Eq. (A5):

$$\frac{[\mathrm{Fe_i^0}]}{[\mathrm{Fe_i^+}]+[\mathrm{Fe_i^0}]} = \frac{1}{\frac{1}{2}\exp\left[(E_{\mathrm{D}}-E_{\mathrm{F}})/k_{\mathrm{B}}T\right]+1} \quad \Leftrightarrow \quad \text{(A6)}$$

$$[\mathrm{Fe_i^+}]+[\mathrm{Fe_i^0}] = [\mathrm{Fe_i^0}]\left\{\frac{1}{2}\exp\left[(E_{\mathrm{D}}-E_{\mathrm{F}})/k_{\mathrm{B}}T\right]+1\right\} \quad \Leftrightarrow \quad \text{(A7)}$$

$$\frac{[\mathrm{Fe_i^+}]}{[\mathrm{Fe_i^0}]}+1 = \frac{1}{2}\exp\left[(E_{\mathrm{D}}-E_{\mathrm{F}})/k_{\mathrm{B}}T\right]+1 \quad \Leftrightarrow \quad \text{(A8)}$$

$$\frac{[\mathrm{Fe_i^+}]}{[\mathrm{Fe_i^0}]} = \frac{1}{2}\exp\left[(E_{\mathrm{D}}-E_{\mathrm{F}})/k_{\mathrm{B}}T\right]. \quad \text{(A9)}$$